nature portfolio

https://doi.org/10.1038/s41586-025-10015-z

Supplementary information

Projected impacts of climate change on malaria in Africa

In the format provided by the authors and unedited

Supplementary Information: Projected impacts of climate change on malaria in Africa

Tasmin L. Symons, Alexander Moran, Ann Balzarolo, Camilo Vargas, Mairi Robertson, Jailos Lubinda, Adam Saddler, Michael McPhail, Joseph Harris, Jennifer Rozier, Annie Browne, Punam Amratia, Amelia Bertozzi-Villa, Samir Bhatt, Ewan Cameron, Nick Golding, Abdisalan M. Noor, Susan F. Rumisha, Matthew D. Palmer, David L. Smith, Daniel J. Weiss, Naomi Desai, David Potere, Nicholas Sukitsch, Wendy Woods, Peter W. Gething

Contents

Overview

Each section in this Supplementary Information provides additional detail to the associated section of the Extended Methods (and numbered box in Extended Data Figure 1) in the Main Text. Although some text has been duplicated for readibility, this document is designed to be read in conjunction with the Main Text and Extended Methods.

1 Preparation of consistent geotemporal climatologies, 2000-2050

1.1 Historical climate data

Raster layers of past climate variables were assembled at 2.5 arcminute resolution (approximately 5 x 5 km at the equator), with temporal resolutions dependant on the product. All raster products were aligned to a standardised reference grid and gap-filled [1]. The choice of variables considered in this analysis was motivated by (a) existing variable selection exercises applied to our PfPR response data [2] intersected with (b) availability as native outputs of CMIP6 model ensemble members, for robustness of forward projections. Relative humidity was calculated from vapour air pressure and temperature. Table 1 summarises the past climate variables and sources used in this analysis, as well as sources of the various contextual factors discussed in the main text.

Model component	Variable	Source	Reference
Malaria ecology	Rainfall	CHIRPS	Funk, C., Peterson, P., Landsfeld, M. et al. (2015) The climate hazards infrared precipitation with stationsa new environmental record for monitoring extremes. Sci Data 2, 150066 [3] doi.org/10.1038/sdata.2015.66

	Vapour Air Pressure	CRU-TS	Harris, I., Osborn, T.J., Jones, P. et al. (2020) Version 4 of the CRU TS monthly high-resolution gridded multivariate climate dataset. Sci Data 7, 109 [4] doi.org/10.1038/s41597-020-0453-3
	Tasselled Cap Wetness	MODIS	Lobser, S. E. and Cohen, W. B. (2007) MODIS tasselled cap: land cover characteristics expressed through transformed MODIS data. International Journal of Remote Sensing. 28(22): 5079-5101 [5] doi.org/10.1080/01431160701253303
	Temperature	Worldclim	Fick, S.E. and Hijmans, R.J. (2017) WorldClim 2: new 1km spatial resolution climate surfaces for global land areas. International Journal of Climatology 37 (12): 4302-4315 [6] doi.org/10.1002/joc.5086
Improved housing	Aridity	CGIAR-CSI	Zomer, R.J., Xu, J. and Trabucco, A. (2022) Version 3 of the Global Aridity Index and Potential Evapotranspiration Database. Sci Data 9, 409 [7] doi.org/10.1038/s41597-022-01493-1 Data file retrieved from doi.org/10.6084/m9.figshare.7504448.v5
	Friction	MAP	`data.malariaatlas.org`[8]
	GDP	-	Murakami, D., Yoshida, T., and Yamagata, Y. (2021). Gridded GDP projections compatible with the five SSPs (shared socioeconomic pathways). Frontiers in Built Environment, 7, 760306 [9] doi.org/10.3389/fbuil.2021.760306 Data file retrieved from doi.org/10.6084/m9.figshare.12016506.v1
	Irrigated Areas	MAP	`data.malariaatlas.org`[8]
Malaria control	Access to effective anti-malarial treatment	MAP	`data.malariaatlas.org`
	IRS coverage	MAP	`data.malariaatlas.org`[8]
	ITN coverage	MAP	`data.malariaatlas.org`[8]

	SMC coverage	MAP	data.malariaatlas.org[8]
Flood modelling	Basin boundaries	HydroBASINS	Lehner, B. and Grill G. (2013) Global river hydrography and network routing: baseline data and new approaches to study the worlds large river systems. Hydrological Processes, 27(15): 21712186 [10] doi.org/10.1002/hyp.9740
	Climate variables	CHIRPS, CRU-TS, MODIS, Worldclim	As above, [3–6]
	Climate zones	-	Kottek, M., Grieser, J. Beck, C. et al. (2006) World Map of the Köppen-Geiger climate classification updated. Meteorol. Z., 15, 259-263 [11] doi.org/10.1127/0941-2948/2006/0130. Data file retrieved from https://koeppen-geiger.vu-wien.ac.at/present.htm
	Flood return period maps	Fathom	fathom.global
	Flow accumulation map	HydroSHEDS	Lehner, B., Verdin, K., Jarvis, A. (2008) New global hydrography derived from spaceborne elevation data. Eos, Transactions, American Geophysical Union, 89(10): 9394 [12] doi.org/10.1029/2008eo100001 Data file retrieved from https://www.hydrosheds.org/hydrosheds-core-downloads
	Historical flood dates	Dartmouth Flood Observatory	floodobservatory.colorado.edu

Historical flood extents	Floodbase	Tellman, B., Sullivan, J.A., Kuhn, C. et al. (2021) Satellite imaging reveals increased proportion of population exposed to floods. Nature 596, 8086 [13] doi.org/10.1038/s41586-021-03695-w Data file retrieved from https://global-flood-database.cloudtostreet.ai/
Land cover	MODIS	Friedl, M., Sulla-Menashe, D. (2022). MODIS/Terra+Aqua Land Cover Type Yearly L3 Global 500m SIN Grid V061 [Data set]. NASA EOSDIS Land Processes Distributed Active Archive Center [14] doi.org/10.5067/MODIS/MCD12Q1.061
Normalized Difference Vegetation Index (NDVI)	USGS	Vermote, E., Justice, C., Claverie, M., and Franch, B. (2016) Preliminary analysis of the performance of the Landsat 8/OLI land surface reflectance product. Remote Sensing of Environment, 185, 46-56 [15] doi.org/10.1016/j.rse.2016.04.008
Soil composition	ISRIC	Batjes N.H., Calisto L. and de Sousa L.M. (2024) Providing quality-assessed and standardised soil data to support global mapping and modelling (WoSIS snapshot 2023). Earth Syst. Sci. [16] doi.org/10.5194/essd-16-4735-2024 Data file retrieved from doi.org/10.17027/isric-wdcsoils-20231130
Topology (elevation)	NCEI	NOAA National Centers for Environmental Information. 2022: ETOPO 2022 15 Arc-Second Global Relief Model. NOAA National Centers for Environmental Information [17] doi.org/10.25921/fd45-gt74

	Waterbodies	HydroSHEDS	Lehner, B. and Döll, P. (2004) Development and validation of a global database of lakes, reservoirs and wetlands, Journal of Hydrology (296) 1-22 [18] doi.org/10.1016/j.jhydrol.2004.03.028.
Cyclone modelling	Climate variables	CHIRPS, CRU-TS, MODIS, Worldclim	As above
	Historic cyclone tracks	IBTrACS	Knapp, K. R., M. C. Kruk, D. H. Levinson, et al. (2010) The International Best Track Archive for Climate Stewardship (IBTrACS): Unifying tropical cyclone best track data. Bull. Amer. Met. Soc. (91), 363–376 [19] doi.org/10.25921/82ty-9e16
	Sea level pressure	ERA5	Hersbach, H., Bell, B., Berrisford, P.,et al. (2023) ERA5 hourly data on single levels from 1940 to present. Copernicus Climate Change Service (C3S) Climate Data Store (CDS) [20] doi.org/10.24381/cds.adbb2d47
	Synthetic cyclone tracks	IRIS	Sparks, N. and Toumi, R. (2024) The Imperial College Storm Model (IRIS) Dataset. Sci Data 11, 424 [21] doi.org/10.1038/s41597-024-03250-y Data file retrieved from doi.org/10.6084/m9.figshare.c.6724251.v1
	Wind speed	ERA5	Hersbach, H., Bell, B., Berrisford, P.,et al. (2023) ERA5 hourly data on single levels from 1940 to present. Copernicus Climate Change Service (C3S) Climate Data Store (CDS) [20] doi.org/10.24381/cds.adbb2d47
Disruption	Friction	MAP	data.malariaatlas.org[8]

	Health facility geolocations	MAP	Weiss, D.J., Nelson, A., Vargas-Ruiz, C.A., et al. (2019) Global maps of travel time to healthcare facilities. Nat Med. 26(12):1835-1838 [22] doi.org/10.1038/s41591-020-1059-1 Data file retrieved from https://malariaatlas.org/project-resources/accessibility-to-healthcare/
	Road networks	OpenStreetMap	OpenStreetMap contributors, Data file retrieved from https://download.geofabrik.de/africa-240101.osm.pbf [23]
Population	Historical	Worldpop	WorldPop (www.worldpop.org - School of Geography and Environmental Science, University of Southampton; Department of Geography and Geosciences, University of Louisville; Departement de Geographie, Universite de Namur) and Center for International Earth Science Information Network (CIESIN), Columbia University (2018). Global High Resolution Population Denominators Project - Funded by The Bill and Melinda Gates Foundation (OPP1134076). doi.org/10.5258/SOTON/WP00675
	SSP245 projection	-	Wang, X., Meng, X. and Long, Y. (2022) Projecting 1 km-grid population distributions from 2020 to 2100 globally under shared socioeconomic pathways. Sci Data 9, 563 [24] doi.org/10.1038/s41597-022-01675-x Data file retrieved from doi.org/10.6084/m9.figshare.19608594.v2

Table 1: **Geotemporal data used in this analysis, with references**. Where variables are products obtained from ongoing projects, the Source column provides the (abbreviated) name of the product or - when the variable refers to one of many products created by the same project - the (abbreviated) project name. Details of the CMIP6 multi-model ensemble members used in this study are described in Table 2.

1.2 CMIP6 projections

Projections of precipitation, relative humidity and temperature (max and min) were obtained from the NASA Earth Exchange Global Daily Downscaled Projections (NEX-GDDP-CMIP6) [25] . These data consist of 0.25 degree downscaled daily CMIP6 multi-model ensemble outputs for historical (2000-2014) and SSP projection (2015-2079) eras.

Although these data were pre-downscaled and bias-corrected, we applied a final delta correction [26] to align with the gap-filled gridded variables listed in Table 1 as follows. First, synoptic 2001-2014 averages were derived for the variables in Table 1 and Table 2 (corresponding to the period of 'historical' CMIP6 data). After unit transformation and aggregation to monthly resolution, SSP-based projections for each model were differenced against their 2001-2014 model synoptic mean (in absolute space for temperature, and relative for precipitation and relative humidity). The resulting deltas were then applied to observed synoptic means (from Table 1 products) to produce projected climate variables aligned with our training data – i.e. we use our 2001-2014 observed variables from Table 1 as a 'baseline'. This simple calibration procedure preserves relative change in variables compared to their historical baseline as each SSP proceeds to 2050, whilst mitigating deviation between the 'historical' Global Climate Model (GCM) outputs (which are not necessarily accurate predictions of past climate) and the observed climate variables used to train the malaria model [26].

Institution	Model	Reference
CSIRO-ACCESS (Australia)	ACCESS-CM2*	Bi et al. (2020) doi.org/10.22033/ESGF/CMIP6.2285
CSIRO (Australia)	ACCESS-ESM1-5	Ziehn et al. (2020) doi.org/10.22033/ESGF/CMIP6.2291

Canadian Centre for Climate Modelling and Analysis (Canada)	CanESM5	Swart et al. (2019) doi.org/10.22033/ESGF/CMIP6.1317 doi.org/10.22033/ESGF/CMIP6.10207
Centro Euro-Mediterraneo sui Cambiamenti Climatici (Italy)	CMCC-ESM2	Cherchi et al. (2019) doi.org/10.22033/ESGF/CMIP6.3825 doi.org/10.22033/ESGF/CMIP6.3887 doi.org/10.22033/ESGF/CMIP6.3889 doi.org/10.22033/ESGF/CMIP6.3890 doi.org/10.22033/ESGF/CMIP6.3896
EC-Earth Consortium (12 European countries)	EC-Earth3-Veg-LR*	Doescher et al. (2020) doi.org/10.22033/ESGF/CMIP6.727
NOAA-Geophysical Fluid Dynamics Laboratory (USA)	GFDL-ESM4	Held et al. (2019), Dunne et al. (2020) doi.org/10.22033/ESGF/CMIP6.1414 doi.org/10.22033/ESGF/CMIP6.9242
Institute for Numerical Mathematics (Russia)	INM-CM4 INM-CM5	Volodin et al. (2017, 2018) doi.org/10.22033/ESGF/CMIP6.12321 doi.org/10.22033/ESGF/CMIP6.12322
National Institute of Meteorological Sciences, Korea Meteorological Administration (South Korea)	KACE-1-0-G	Lee et al. (2020) doi.org/10.22033/ESGF/CMIP6.2241
Max Planck Institute for Meteorology, Deutsches Klimarechenzentrum), Deutscher Wetterdienst (Germany)	MPI-ESM1-2-HR MPI-ESM1-2-LR*	Mauritsen et al. (2019), Mueller et al. (2018) doi.org/10.22033/ESGF/CMIP6.2450 doi.org/10.22033/ESGF/CMIP6.1869 doi.org/10.22033/ESGF/CMIP6.793
Meteorological Research Institute (Japan)	MRI-ESM2-0	Yukimoto et al. (2019) doi.org/10.22033/ESGF/CMIP6.638
Norwegian Climate Centre (Norway)	NorESM2-LM NorESM2-MM	Seland et al. (2020), Tjiputra et al. (2020), Counillon et al. (2016) doi.org/10.22033/ESGF/CMIP6.604 doi.org/10.22033/ESGF/CMIP6.608 doi.org/10.22033/ESGF/CMIP6.10894

Table 2: **CMIP6 multi-model ensemble members obtained from NEX-GDDP-CMIP6**. Outputs from these models were downscaled and bias-corrected to create the ensemble of NASA Earth Exchange Global Daily Downscaled Projections (NEX-GDDP-CMIP6) [25] used in this study. Asterisks indicate GCMs used in disruptive impacts ensemble.

After assembly of past and (suitably calibrated) projected climate variables, various combinations were used to produce mechanistically-motivated malaria-climate indices varying more linearly with (logit) *Pf*PR, described below.

2 Modelling of historical and projected climate suitability indices

2.1 Temperature Suitability Index

The constraints of temperature on sporogony and vector lifespan and activity lead to a non-linear relationship between temperature and malaria transmission [27]. Too cold, and mosquito biting rate decreases whilst the Extrinsic Incubation Period (EIP) of the parasite becomes prohibitively long; too hot, and the mosquito host dies before the transmission cycle can complete. The biological mechanism of this relationship is relatively well-understood, and may be linearised via a mechanistic model generating a ‘temperature suitability index’ [27], which combines the degree-day model of EIP with parametric temperature-biting-rate and temperature-survival curves for Anopheles vectors. To make computation of multiple future trajectories tractable, a simplified degree-day TSI was computed: relative Vectorial Capacity as a function of temperature T is given by

$$Z(T) = \frac{\exp\left\{-g(T)n(T)\right\}}{g(T)^2}, \tag{1}$$

where $g(T)$ is the death rate of adult mosquitos given by

$$g(T) = \frac{1}{-4.4 + 1.31T - 0.03T^2}, \tag{2}$$

(see Gething *et. al.* [27] for parametrisation) and $n(T)$ is the temperature-dependent EIP in degree-days.

Sporogony occurs after a fixed number of degree-days φ when the temperature exceeds T_{min}:

$$n(T) = \begin{cases} \frac{\varphi}{T - T_{\text{min}}}, & T > T_{\text{min}}, \\ \infty & T \leq T_{\text{min}}. \end{cases} \tag{3}$$

Recent studies [28, 29] have demonstrated that the orthodox parameters $\varphi = 111$ and $T_{\text{min}} = 16$ overestimate the EIP at low temperatures, and that peak parasite development may occur at a lower temperature than previously suggested. Using lab-based measurements of sporogony in *Anopheles gambiae* mosquitos reared at a range of temperatures, Suh *et. al.*[29] recently suggested a new temperature-dependent EIP curve, based on a mechanistic model allowing stochastically varying EIP among mosquito cohorts [28].

For compatibility with Gething *et. al.*'s [27] method for estimating $Z(T)$, we fit the parameters of Equation (3) to EIP$_{50}$ model results extracted from [29], resulting in updated degree-day parameters $\varphi = 92.95$ and $T_{\text{min}} = 15.56$. Using these new parameters, EIP was 64.5 days at 17C, falling to 6.92 days at 29C. The resulting normalised TSI curve is shown in Figure 1.

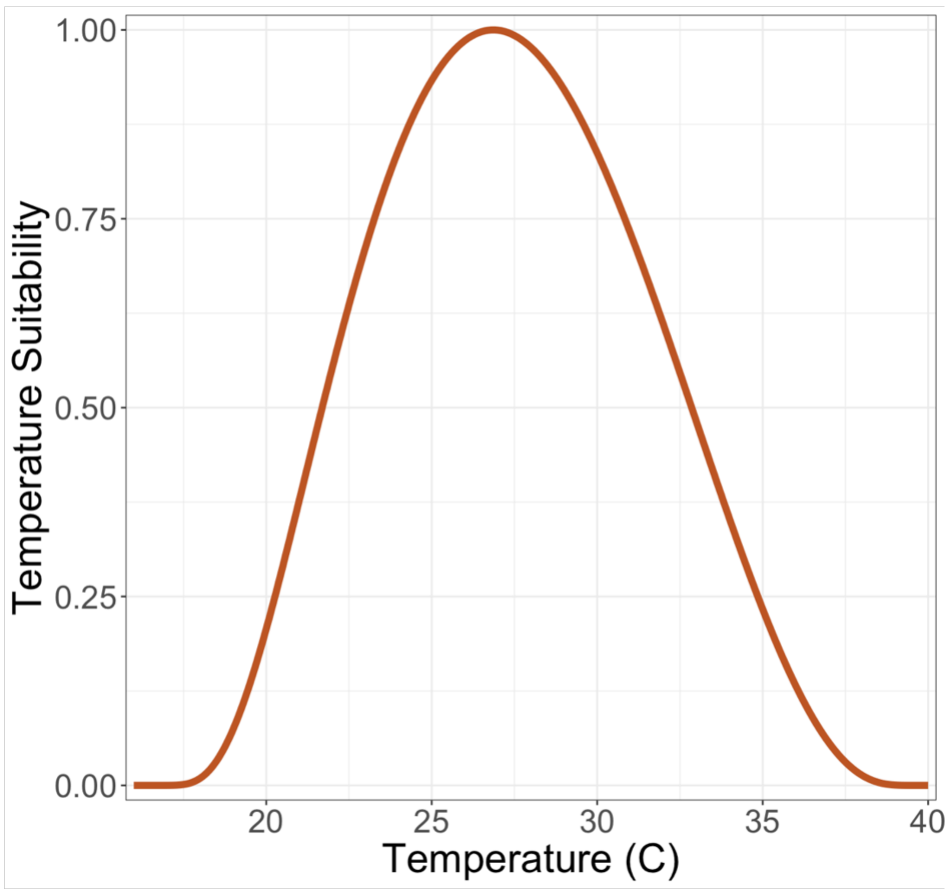

Figure 1: Temperature suitability index (TSI, or relative Vectorial Capacity) as a function of mean temperature in C. TSI peaks at 26.8C, falling to $<$0.000001 at 16.4C and 39.69C. These bounds, and the shape of the curve, are consistent with other proposed relative Vectorial Capacity estimates [30, Fig 5e.].

2.2 Habitat Suitability

2.2.1 Rainfall habitat suitability

Abundance of *Anopheles* mosquitoes is strongly correlated with rainfall and subsequent formation of transient habitat suitable for oviposition [31]. Rainfall-derived habitats (puddles) are non-permanent, with their rate of evaporation determined by ambient temperature and humidity. The existence of such transient larval habitat is a function of temperature, relative humidity, and rainfall. Eckhoff [32] proposed an autoregressive structure for the existence of such transient larval habitats (normalised to have area 1) as a function of rainfall (R), temperature (T) and humidity (H) at time t.

$$\text{Habitat}(t) = R_\tau + \frac{1}{\delta_t}\text{Habitat}(t-1), \tag{4}$$

$$\delta_t = C \exp\left\{-\frac{1}{T_t + 273.15}\right\} \sqrt{\frac{1}{T_t + 273.15}}(1 - H_t), \tag{5}$$

i.e. habitat is formed by rain before evaporating at rate δ_t. We refer to Eckoff [32] for a full exposition of C, a composite of various physical constants determining the temperature-dependent evaporation rates. Figure 2 shows $1/\delta_t$ for a range of temperature and humidity. As relative humidity rises to 100%, the rate of evaporation falls to zero, whilst as it falls to 0 the rate of evaporation rises to a temperature-dependent maximum.

In lieu of parametrising a fully mechanistic habitat model as in Equation (1), for tractability we instead constructed a proxy function which (a) captures the fundamental characteristics of the above model to appropriately constrain an empirically derived relationship; and (b) is compatible with available climate variables – both remotely sensed historic and GCM output projections. Per Eckoff [32], $1/\delta_\mathrm{t}$ defines the half-life of habitat duration as a function of temperature T_t and relative humidity H_t. We converted this into an expected duration of habitat by setting

$$\text{dur}_\tau = \frac{1}{\log 2}\frac{1}{\delta_t}. \tag{6}$$

Then, with m a month-year, $|m|$ denoting the length of m in days, and R_d daily rainfall, we proxied

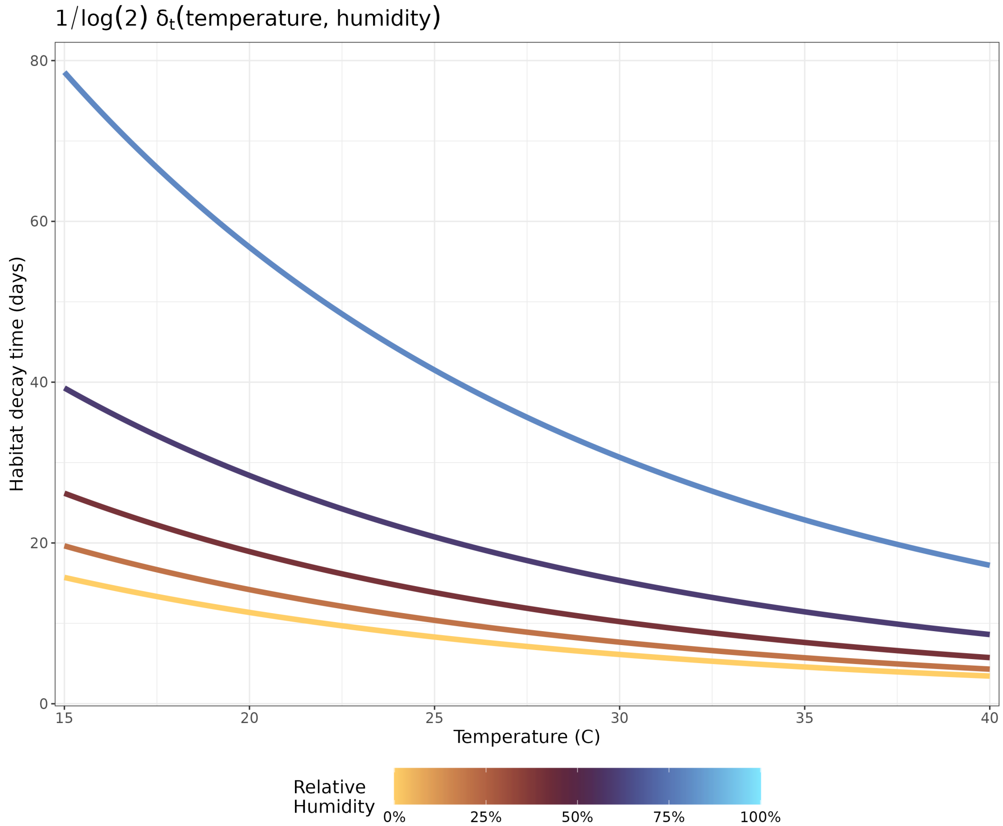

Figure 2: The decay rate of transient larval habitat as a function of temperature and relative humidity. Each coloured line represents a fixed relative humidity.

Equation (4) with a monthly 'rainfall suitability index' (RSI):

$$\text{RSI}(m) = \sum_{d \in m} \frac{R_d}{|m|} \min(\text{dur}_m, |m| - d) + \tag{7}$$

$$\sum_{d \in m-1} \frac{R_d}{|m-1|} \max(0, \text{dur}_m - |m-1| + d)) \mathbb{I}(\text{dur}_{m-1} > |m-1| - d) \tag{8}$$

abusing notation somewhat by writing dur_m to denote the mean of $\text{dur}_t, t \in m$.

The reasoning for Equation (7) is as follows: the first sum is weighted cumulative rainfall where the weights given by the proportion of the month the resulting habitat endures, ie the shorter of (a) the duration of the habitat; or (b) the number of days remaining in the month. The second sum, meanwhile, accounts for habitats persisting from the previous month – lagged daily rainfall totals are weighted by their expected remaining duration, conditioned on the habitat existing on the final day of month $m-1$. The maximum prevents negative weights in that case that $\text{dur}_m \neq \text{duration}_{m-1}$. Thus, Equation (7) captures key features of Equation (4):

- Rainfall dependent habitat creation, with temperature and humidity dependent habitat destruction;
- As $H_m \to 0$, $\min(\text{dur}_m, |m| - d) \to 0$;
- As $H_m \to 1$, $\min(\text{dur}_m, |m| - d) \to |m| - d$ and so habitat availability grows monotonically with additional rainfall – especially in the case where $H_{m-1} \to 1$ also, so that $\mathbb{I}(\text{dur}_{m-1} > |m-1| - d) = 1$ for most days in $m-1$.

2.2.2 Permanent habitat suitability

In addition to habitat derived from local rainfall, habitat arises as the result of longer-term water flux supporting permanent habitats [33]. To account for this, we derived an 'excess wetness' surface from MODIS Tassel-Capped Wetness (TCW) observations. TCW is the wetness component of the Tasselled Cap transformation of remotely sensed imagery, measuring soil and vegetation moisture and surface water [5]. First, a linear regression between between synoptic average TCW and cumulative local rainfall over the preceding 3 months was fit

$$\widetilde{\text{TCW}}_{s,m} = \alpha + \beta_1 \text{asinh}(\text{rain}_{s,[m-2:m]}) \tag{9}$$

where s denotes a grid-cell and m is calendar month. The residuals – ie wetness not explained by recent rainfall – were then calculated for each month

$$r = \text{TCW}_{s,m} - \widetilde{\text{TCW}}_{s,m}, \tag{10}$$

to proxy the presence of permanent habitat.

2.3 Habitat Suitability Index

Derived permanently available larval habitat r was then scaled to match the relative magnitude of transient habitat availability RSI(m), and combined with it (by taking the grid-cell-wise maximum) to create a final habitat availability index surface HSI(m).

Availability of larval habitat acts directly on EIR, rather than *Pf*PR. Thus, prior to modelling, the final habitat availability index was inverse-hyperbolic-sine transformed, motivated by (a) the known log-linear relationship between EIR and observed parasite rate and (b) the presence of zeros in computed rainfall suitability indicating total absence of rainfall-derived habitat, precluding log transformation.

The relationship between these climate indices and observed *Pf*PR is shown in Extended Data Figure 7 in the main text.

3 Preparation of historical geotemporal housing, intervention, and contextual data

In addition to the climate, malaria transmission is strongly mediated by human factors – socio-economics [34] and malaria control [35]. Empirical analysis of the impact of climate on malaria transmission must therefore control for these factors. Here we considered (a) urbanicity and wealth proxied by access to improved housing and (b) coverage of four key classes of malaria control: insecticide treated nets (ITNs); access to effective treatment with antimalarials (EFT); insecticidal residual spraying (IRS); and seasonal malaria chemoprevention (SMC).

3.1 Malaria control

Geospatial estimates of historic (2000-2022) insecticidal bednet (ITN), indoor residual spray (IRS), seasonal malaria chemoprevention (SMC) and antimalarial treatment coverage were obtained from the Malaria Atlas Project, corresponding to v2023 estimates available at `data.malariaatlas.org` and hence, where their estimates are used by WHO, to World Malaria Report 2023 [36].

Before regression against *Pf*PR ITN use estimates were combined with an estimate of pre-intervention-era parasite rate using a pre-defined interaction term[35],: for ITN coverage X_{ITN} and pre-intervention-era *Pf*PR$_{\text{2-10}}$ p take

$$\mathcal{I}(X_{\text{ITN}}, p) = (p^{0.4} - p^{20}) X_{\text{ITN}}^{1.5p}. \tag{11}$$

The baseline estimates of thus transformed ITN coverage and (untransformed) access to effective antimalarial treatment used in this analysis are plotted in Figure 20.

3.2 Relative abundance of vector species

Malaria ecology varies by species, with the relationship between the environmental suitability indices described above and malaria transmission levels expected to vary between settings with different dominant vectors, even after controlling for malaria control and socioeconomic factors [37]. To account for this we fit species-specific terms in the model, with predictions based on relative abundance of the three dominant vectors in sub-Saharan Africa: *Anopheles gambiae (s.s. and coluzzi)*, *Anopheles funestus*, and *Anopheles arabiensis*.

The range of species overlaps, making relative abundance – rather than simply dominance a more nuanced metric. Estimates of relative abundance of each species were obtained from Sinka *et al* [37], providing for each 5 x 5 km grid cell a three-way weighting of malaria vector species. These estimates were based on observational data for the period 1985-2010, but here we make the simplifying assumption that species relative abundance does not change substantially through time.

3.3 Socioeconomics

An improved house is defined (see Tusting *et. al.* [38]) by the absence of all four of

- Unimproved water supply: a water supply is improved if it is piped into the dwelling/yard/neighbour, or drawn from a public well
- Unimproved sanitation: sanitation is improved if a dwelling's toilet is flushing, composting or chemical
- Overcrowding (more than three people per bedroom)
- Walls/floor/roof made of natural or unfinished materials.

A predictive geostatistical model of community-level prevalence of improved housing was developed for this analysis, following the methodology in Tusting et al [38]. 1,083,386 geo-located observations of house fabric and WASH facilities were collated from the DHS program [39] and categorised into improved/unimproved per the above rubric. Data were then grouped by geo-located cluster to give 43,926 binomial samples of prevalence of improved housing between 2005 and 2022. These were linked to raster surfaces of aridity, traversibility, irrigation, population and GDP (see Table 1).

Full Gaussian Process regression was approximated using $k = 500$ Random Fourier Features [40]. N$(0, 1)$ priors were set on the Random Fourier Feature slopes, and an $N(-4, 4)$ prior on the intercept. A beta-binomial likelihood was used with overdisperson prior $\phi \sim$ Gamma$(0.05, 0.1)$. The model was fit using the Adam optimiser as implemented in the `opt` function in greta 0.4.3.9. Learning rate was set to 0.025, max iterations to 1000, and tolerance to 0.001. Parameters are shown in Table 3. MSE was 0.03, correlation 0.78. 2022 estimates of prevalence of improved housing are shown in Figure 3.

intercept	ϕ						
-0.523	3.604						
$\log(bw_1)$	$\log(bw_2)$	$\log(bw_3)$	$\log(bw_4)$	$\log(bw_5)$	$\log(bw_6)$	$\log(bw_7)$	$\log(bw_8)$
0.112	-0.181	0.011	-0.479	-0.614	-0.834	0.159	0.526

Table 3: **Fitted parameters of prevalence of improved housing model.**

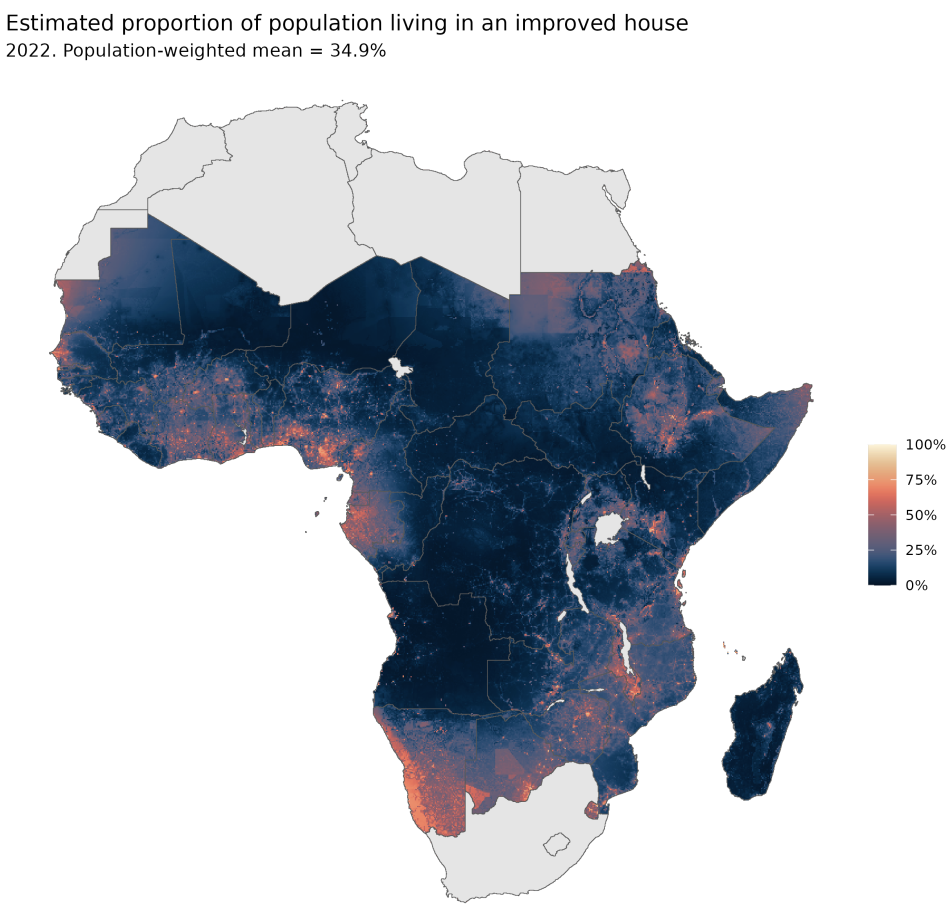

Figure 3: Estimated prevalence of improved housing, 2022. This was used as baseline, which was perturbed by displacement/disruptions associated with extreme weather events as described in the methods. Administrative boundaries were obtained from the Malaria Atlas Project [8].

4 Preparation of historical malaria response data

49,994 geo-located observations of Plasmodium falciparum parasite rate (*Pf*PR) were collated from DHS program [39] and systematic literature review by the Malaria Atlas Project [8], representing 2.54 million individuals tested between 1995 and 2021 across 41 African countries. These data were standardised for age (to 2-10 years) and diagnostic type (to gold-standard light microscopy) using existing models [41, 42], consistent with established approaches to modelling these data geospatially [43]. The median cluster sample size was 20, inter-quartile range 11-50.

4.1 Data summary

Figure 4 summarises the spatio-temporal distribution of standardised *Pf*PR$_{2\text{-}10}$ data used to fit our model.

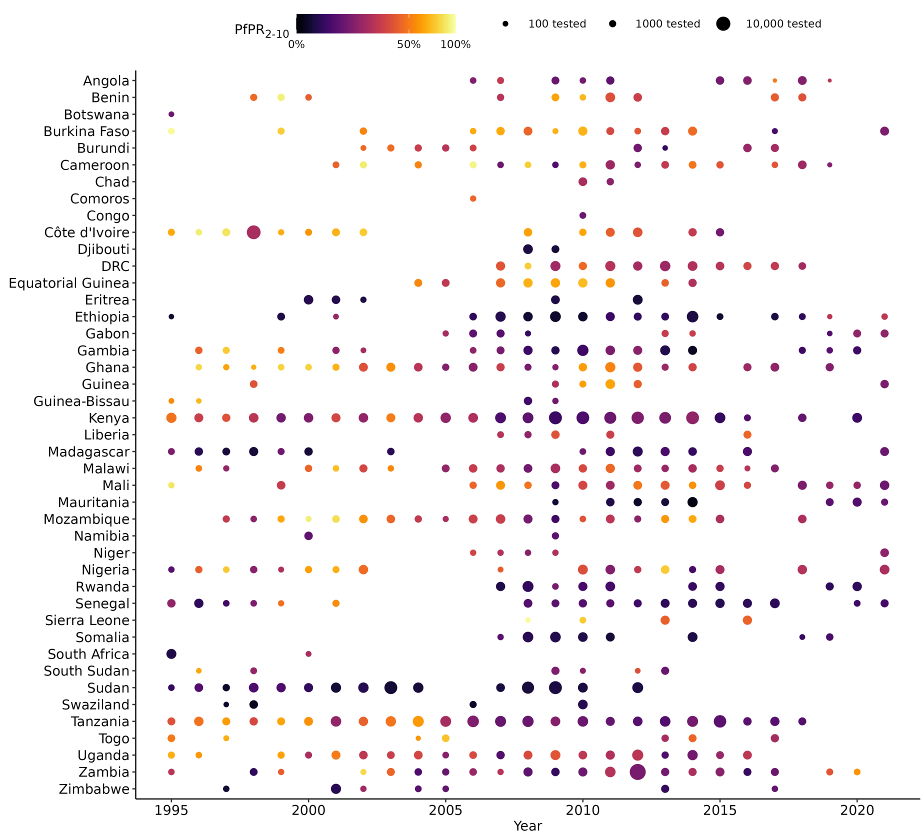

Figure 4: Summary of *Pf*PR data used to train malaria model. Country-years with observations are denoted by dots, with the size of the dot showing the number of samples collected in that country-year. The colour shows the average *Pf*PR, with the colour ramp square-root transformed to show variation in the data.

4.2 Response versus covariate data

To complement Extended Data 7, which shows the relationships between our modelled environmental suitability indices and observed *Pf*PR at various levels of suppression, here we display the raw response-predictor relationships considered in this analysis (Figure 5). The nonlinear relationship between ITN use and *Pf*PR is accounted for using a pre-defined interaction term [35] (see Section 3.1, Equation 11).

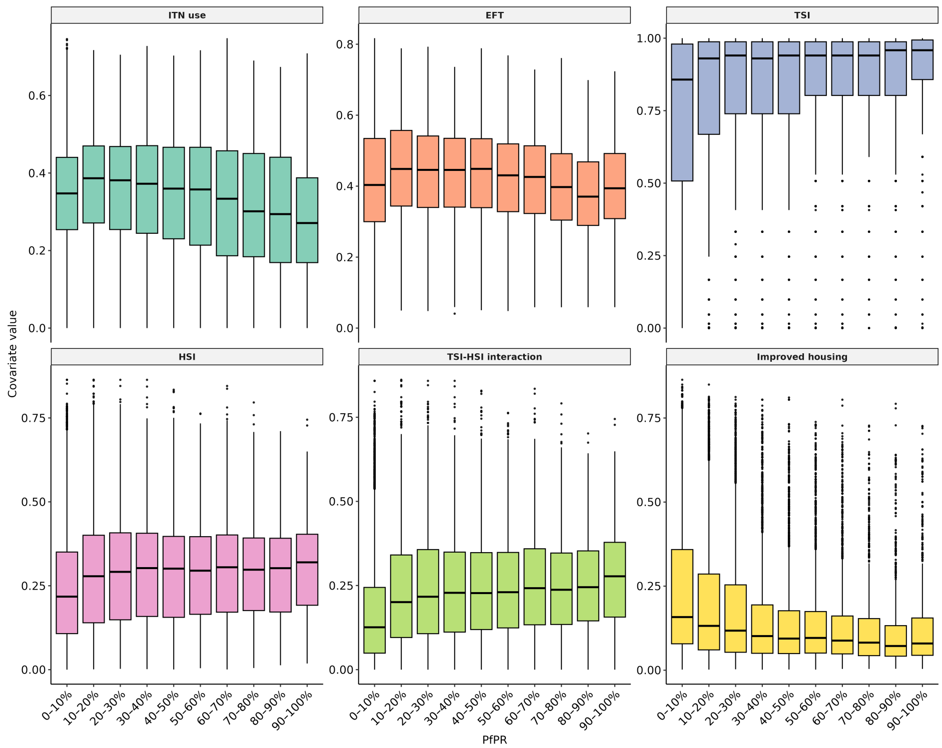

Figure 5: Summary of raw relationships between *Pf*PR data used to train malaria model and the predictor variables used, including interaction between temperature and habitat suitability.

5 Characterising historical climate, housing, intervention and other contextual effects on malaria

5.1 Model details

We used stacked generalisation to regress the predictor variables onto $Pf\mathrm{PR}_{2\text{-}10}$ observations. Stacked generalisation – which ensembles out-of-sample predictions from multiple 'level 0' models as predictors in a final geostatistical model – has been shown to have superior predictive ability to standard model-based geostatistics when applied to $Pf\mathrm{PR}_{2\text{-}10}$, and here allows for more flexible predictor variables to characterise the environment-malaria relationship than seen in previous generalised linear model approaches [44].

Three level 0 models were used in this analysis: a linear model, a generalised additive model, and a boosted regression tree. The three models took the following forms.

Linear model:

For *Pf*PR$_{2\text{-}10}$, observed in location s at time t $y_{s,t}$:

$$\text{elogit}(y_{s,t}) \sim N(\mu_{s,t}, \sigma^2) \tag{12}$$

$$\mu_{s,t} = U_{c[s]} + \sum_{i=1}^{7} \tilde{\beta}_i X_{i,s,t}^{\text{climate}} + \sum_{i=1}^{5} \tilde{\gamma}_i X_{i,s,t}^{\text{contextual}} \tag{13}$$

where elogit is the empirical logit function, U_c was a country specific intercept, $X_{s,t}^{\text{climate}}$ was a seven-column vector consisting of, in pixel s at time t, (i) standardised asinh-transformed HSI, cumulative across two- and three- month lags; (ii) standardised TSI, at one month lag, (iii) their multiplicative interaction; (iv) and (v) *An. arabiensis* relative abundance weighted versions of (i) and (ii); and finally (vi), (vii)*An. funestus* relative abundance weighted versions of (i) and (ii) [ie *An.gambiae* (*s.s.* and *coluzzi*) was taken as our reference species for terms (i) and (ii)]. $X_{s,t}^{\text{contextual}}$ was a five-column vector consisting of prevalence of improved housing; the ITN interaction term described above; IRS coverage; access to effective treatment with an antimalarial; and SMC coverage.

Generalised additive model:

Model formula as for level 0 model (12), with *An. funestus* as reference species, and the linear terms for *An. gambiae* relative abundance weighted HSI, housing, IRS and SMC replaced with penalised cubic splines.

Generalised Boosted Regression:

Model formula as for level 0 model (12), with interaction term removed and replaced with species-specific terms for all three species. Monotonicity constraints were placed on the model terms to prevent spurious results. 1000 trees were fit 1000 trees were fit,, with an interaction depth of four.

These three level 0 models were fit to the *Pf*PR$_{2\text{-}10}$ dataset described above, avoiding over-fitting by using five-fold cross-validation to generate out-of-sample predictions to be used as fixed effects when training the level 1 generaliser model. For tractability, we modified the stacked generalisation approach by, for each level 0 model, generating these hold-out predictions with interventions set to zero. That is, each of the level 0 models provided an (out-of-sample) predictor representing estimated risk in the absence of interventions. Each of the Level 0 models was also fit to the full *Pf*PR$_{2\text{-}10}$ training set to generate gridded predictions (again with interventions set to 0, to produce estimates of intervention-free risk) from the Level 1 geostatistical generaliser model. Parameters of the Level 0 models are shown in Table 4.

Each intervention class was then included in the geostatistical generaliser model as a fixed effect. For location s and time t (in month-years) the primary model can be expressed, for PfPR $y_{s,t}$, as:

$$\text{elogit}\, y_{s,t} \sim \text{Normal}(\eta_{s,t}, \sigma_\epsilon^2) \tag{14}$$

$$\eta_{s,t} = \sum_{i=1}^{3} \beta_i X_{i,s,t} + \sum_{i=1}^{4} \gamma_i I_{i,s,t} + Z_{s,t} \tag{15}$$

where $X_{s,t}$ are the out-of-sample level 0 zero-intervention predictions, $I_{s,t}$ is the vector of malaria control coverage (interacted with baseline *Pf*PR$_{2\text{-}10}$, in the case of ITNs) at pixel s at time t, Z is spatio-temporal random field with separable Matérn-5/2 spatial and AR(1) temporal kernel, and ϵ is uncorrelated measurement error.

Note that the vector $I_{s,t}$ was multiplied by -1, so that the positive effect size estimates γ quoted below in Tables 4 and 5 correspond to *negative* relationships with infection prevalence (as one would expect). Improved housing was not negated, so its negative slopes in Table 4 reflects its negative association with *Pf*PR$_{2\text{-}10}$.

Penalised complexity priors [45] were applied to the spatial field: $P(\rho < \frac{7}{180}\pi) = 0.1$ (a 3d spherical mesh was used) and $P(\sigma_{\text{field}} > \log(1.1)) = 0.01$ and AR(1) temporal component: $P(cor > 0.7) = 0.99$, $P(\sigma_{\text{AR(1)}} > 0.05) = 0.01$. $N(4, 0.1)$ and $N(0.5, 0.1)$ priors were assigned to the ITN interaction and treatment terms, respectively, whilst $N(0.5, 1)$ priors were applied to the other fixed effects. Level 0 model slopes β'_{glm}, β'_{gam} and β'_{brt} were checked to be positive for generalisability when stacked [44], with model performance verified by out-of-sample validation (see below). Following previous approaches to modelling *Pf*PR$_{2\text{-}10}$, we used a Gaussian likelihood and empirical logit transform to ensure well-specified posterior distributions [35]. The level 1 model is thus formally described hierarchically as:

$$\text{elogit}\, y_{s,t} \sim \text{Normal}(\eta_{s,t}, \sigma_\epsilon^2) \tag{16}$$

$$\eta_{s,t} = \sum_{i=1}^{3} \beta_i' X_{i,s,t} + \sum_{j=1}^{4} \gamma_j' I_{j,s,t} + Z_{s,t} \tag{17}$$

$$Z_{s,t} \sim \mathcal{GP}(0, \Sigma_{\text{space}} \otimes \Sigma_{\text{time}}) \tag{18}$$

$$\Sigma_{\text{space}} \sim \text{Matérn}(5/2), \quad \text{PC prior: } P(\text{range} < \tfrac{7}{180}\pi) = 0.1, \quad P(\sigma_{\text{space}} > \log(1.1)) = 0.01 \tag{19}$$

$$\Sigma_{\text{time}} \sim \text{AR(1)}(\rho), \quad \text{PC prior: } P(\rho > 0.7) = 0.99, \quad P(\sigma_{\text{time}} > 0.05) = 0.01 \tag{20}$$

$$\beta_i' \sim N(0,1), \tag{21}$$

$$\gamma_1' \sim N(4, 0.1) \tag{22}$$

$$\gamma_2' \sim N(0.5, 0.1) \tag{23}$$

$$\gamma_j' \sim N(0.5, 1), \quad j = 3, 4. \tag{24}$$

Each observation was modelled as conditionally independent given the underlying fixed effects and latent spatio-temporal process. Whilst this assumption simplified computation and is consistent with previous analyses of these data [35, 44, 46], we did not explicitly account for intra-cluster correlation arising from DHS survey design. Future extensions could incorporate cluster-level random effects accounting for this, although these were computationally infeasible at the spatial and temporal scale of the present analysis.

5.2 Parameters and validation

The final geostatistical model was fit in R 4.2.0 using INLA v22.12.16. The INLA package implements the integrated nested Laplace approximation, an approximate Bayesian inference method [47]. Using INLA, spatial processes on $\mathbb{S}^2$ with Matérn covariances can be easily approximated using sparse representations of the solution to the SPDE which defines the Matérn kernel [48]. Fitted parameters - including hyperparameters for the Gaussian random field - are shown in Table 5. A single model was fit to the entire domain, assuming the unexplained spatial and temporal variation was stationary and isotropic - that is, the spatial and temporal dependence structures were constant across regions. In-sample observed versus fitted correlation was 0.86, root mean squared error was 0.09, mean absolute error was 0.09 (in *Pf*PR space). Mean log CPO, summarising out-of-sample predictive density, with higher values indicating better performance, was

Term	LM slope	GAM slope	BRT relative importance (rank)
interaction_HSI_TSI	0.613	0.941	not included
HSI	0.398	-0.343	not included
TSI	1.004	1.697	not included
arabenisis_TSI	-0.732	-1.408	7
funestus_TSI	0.749	reference	2
gambiae_TSI	reference	-0.988	1
arabenisis_HSI	0.615	0.800	10
funestus_HSI	-0.240	reference	8
gambiae_HSI	reference	cubic spline	3
Improved housing	-2.178	cubic spline	4
ITN interaction†	1.439	0.956	5
EFT†	1.202	3.893	9
IRS†	0.210	cubic spline	6
SMC†	1.169	cubic spline	11

Table 4: **Summary of fitted climate and contextual factor parameters for Level 0 models.** † denotes malaria control variables set to 0 when using these Level 0 models to generate both out-of-sample predictor variables for Level 1 model training and final Level 0 projection surfaces.

	mean	sd	0.025quant	0.5quant	0.975quant
β'_{glm}	0.147	0.057	0.036	0.147	0.258
β'_{gam}	0.324	0.056	0.214	0.324	0.435
β'_{brt}	0.088	0.009	0.070	0.088	0.106
$\gamma'_{\text{interact}}$	1.356	0.098	1.164	1.356	1.549
γ'_{eft}	1.870	0.119	1.637	1.870	2.103
γ'_{irs}	0.505	0.069	0.370	0.505	0.640
γ'_{smc}	0.447	0.065	0.319	0.447	0.575
Precision for the Gaussian observations	1.053	0.007	1.038	1.052	1.067
Range for field	0.040	0.001	0.037	0.040	0.043
Stdev for field	1.378	0.027	1.324	1.378	1.431
GroupRho for field	0.224	0.034	0.156	0.225	0.288

Table 5: **Fitted parameter values from the geostatistical Level 1 model.** Posterior mean, standard deviations, and 2.5%, 50% and 97.5% quantiles are shown for each model parameter.

-1.44, comparable to other models fit to these data [46].

To validate the appropriateness of the Bayesian model's uncertainty estimates, we examined the posterior coverage (Figure 6) and Probability Integral Transform (PIT) histogram (Figure 7). Accounting for measurement noise, cluster-level posterior predictive coverage was 92.1% (i.e. 92.1% of the estimated 95% CI posterior estimates contained the empirical 95% interval of the observations). The PIT showed an approximately uniform distribution, further suggesting the posterior predictive distribution was well-calibrated. Figure 8 shows (a) the histograms of the residuals, with Gaussian density overlaid, and (b) the residual variance across different levels of observed PfPR.

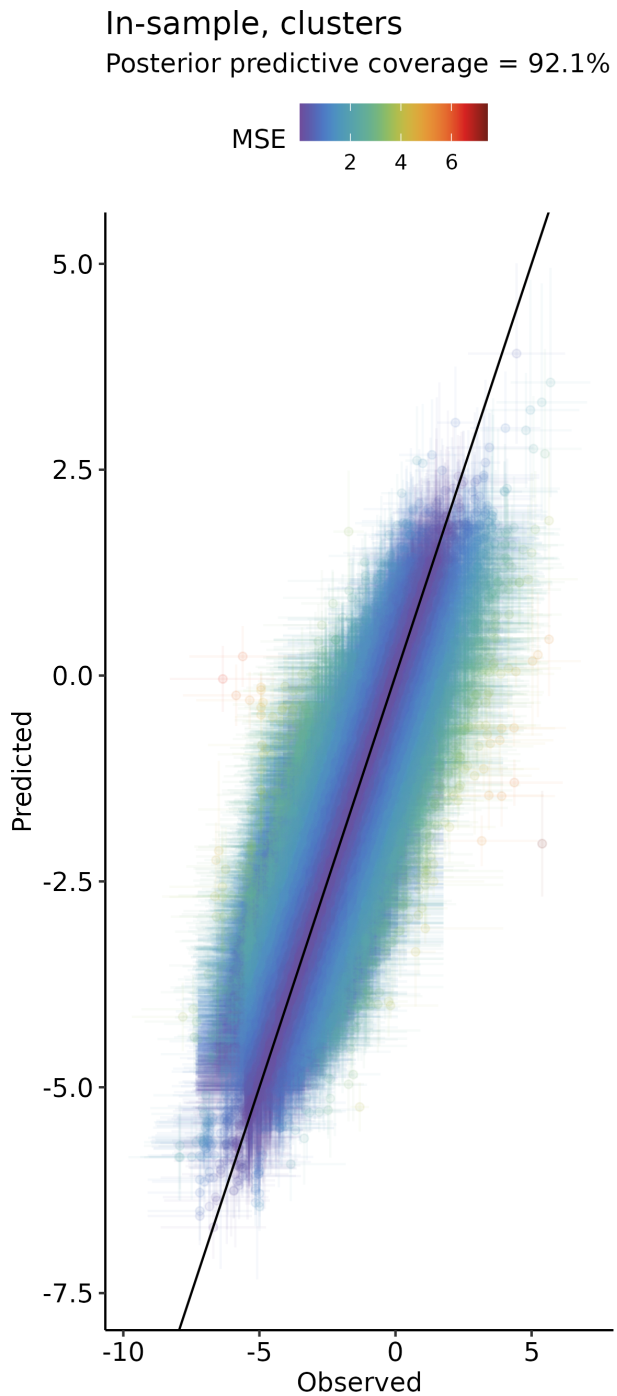

Figure 6: In-sample cluster validation, with measurement noise (horizontal bars) and posterior predictive distribution (vertical bars). Measurement noise was calculated as the approximate 95% interval derived from the empirical-logit variance of the observation, given by Var $= \frac{1}{Y+0.5} + \frac{1}{N-Y+0.5}$, where N is the sample size (when known) and Y the number of successes.

We found no strong association between PfPR and residual variance, suggesting that our assumption of homoskedastic Gaussian error is a reasonable approximation. The semi-variogram of the residuals (Figure 9) indicates no residual spatial autocorrelation due to eg anistropy, suggesting

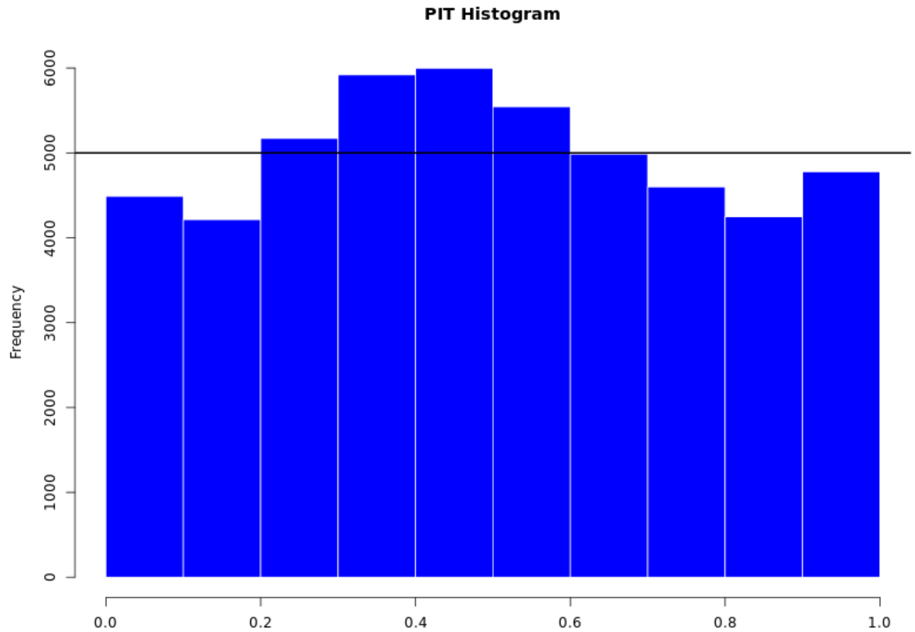

Figure 7: PIT values comparing the observed data to cumulative predictive densities. If the two distributions match the data generating process coincides with the predictive distribution, with the result approximately uniform.

the assumption of global hyperparameters for the spatio-temporal random field is suitable.

Initial verification of out-of-sample predictive performance used five-fold cross-validation, holding out 20% of the training set (i.e. ≈10,000 observations) at each fold. This yielded out-of-sample correlation (in *Pf*PR space) of 0.83, RMSE of 0.14, MAE of 0.10, suggesting the model generalised well and did not overfit. This out-of-sample performance is consistent with other well-fit models of malaria prevalence in Africa [35]. Scatter plots of observed vs predicted outputs, out-of-sample, are shown in Figure 10.

To further interrogate predictive performance of the model under more strident conditions, we held out each of the 72 DHS Program surveys included in this analysis, sequentially. This approach reflects a more challenging extrapolation setting, as the model must predict both spatial and temporal variation without any concurrent observations for calibration. Entire-survey-out-of-sample error metrics were (in *Pf*PR space): RMSE 0.19 and MAE 0.12 at cluster-level, and 0.08 RMSE, 0.05 MAE at survey aggregate – consistent with the out-of-sample errors observed after standard cross-validation described above.

Interval scores [49] for the different types of validation are shown in Table 6: scores are calculated by penalising wide intervals and/or observations falling outside the prediction intervals, given

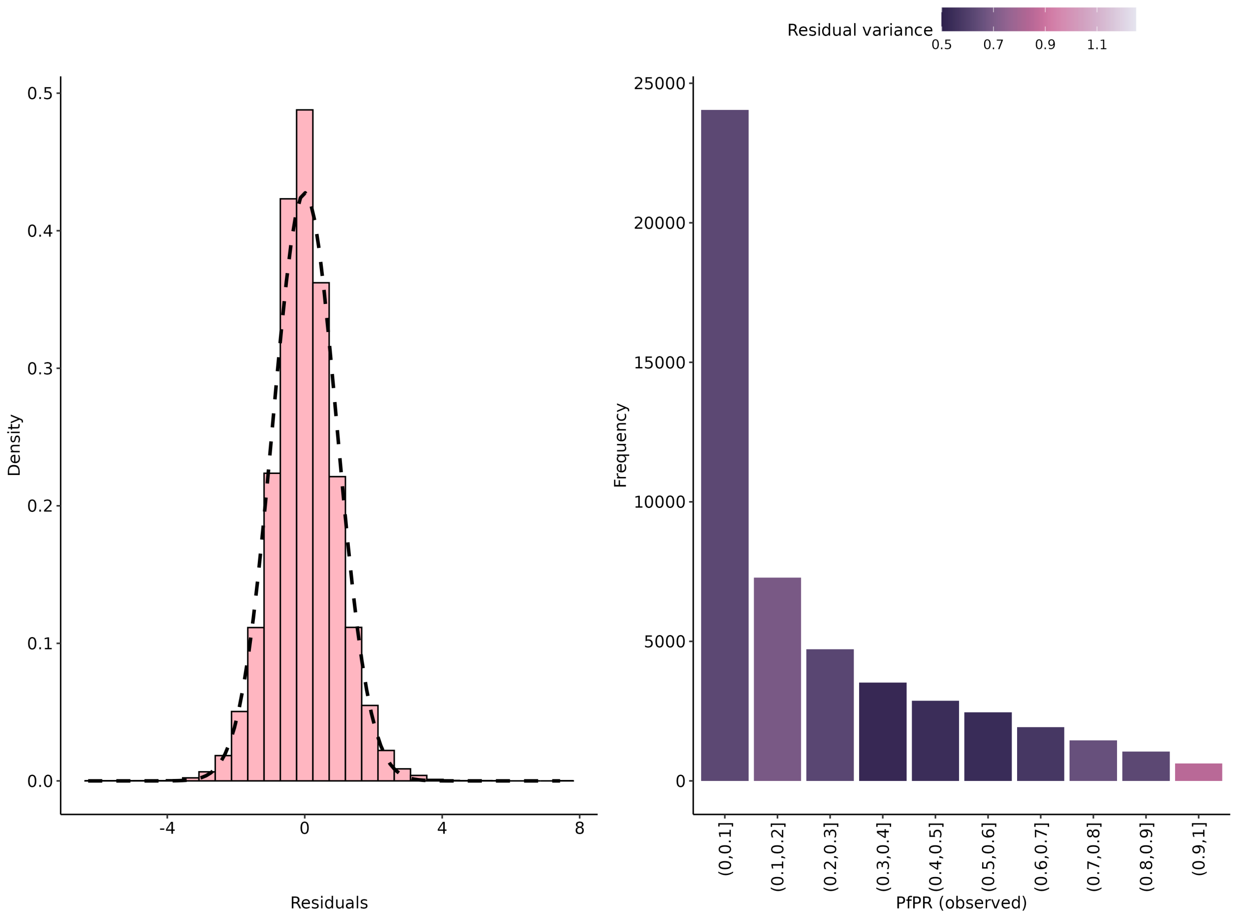

Figure 8: Analysis of residuals of Level 1 geostatistical model. Left-hand panel shows histogram of residuals with a Gaussian distribution overlaid. Right-hand panel shows bins of observations, coloured by the residual variance. Uniformity of colour indicates that residual variance is not strongly influenced by magnitude of observation

by, for $(1-\alpha)$ predictive interval $[l, u]$ and observed value y:

$$I(l, u, |y) = (u - l) + 2/\alpha(l - y)\mathbb{I}_{y<l} + 2/\alpha(y - u)\mathbb{I}_{y>l} \tag{25}$$

A lower interval score indicates 'better' model performance, rewarding narrow intervals which cover the observations.

Finally, we assessed the sensitivity of the learned fixed effects to held-out data. Figure 11 shows the mean and 95% CI of each of the coefficients learned in the Level 1 model, with points overlaid for mean coefficients generated by each validation model holding out various subsets of the data. There is minimal movement in the coefficients, relative to their posterior intervals. As expected, most variation occurred when excluding *Pf*PR observations collected via MAP's rolling

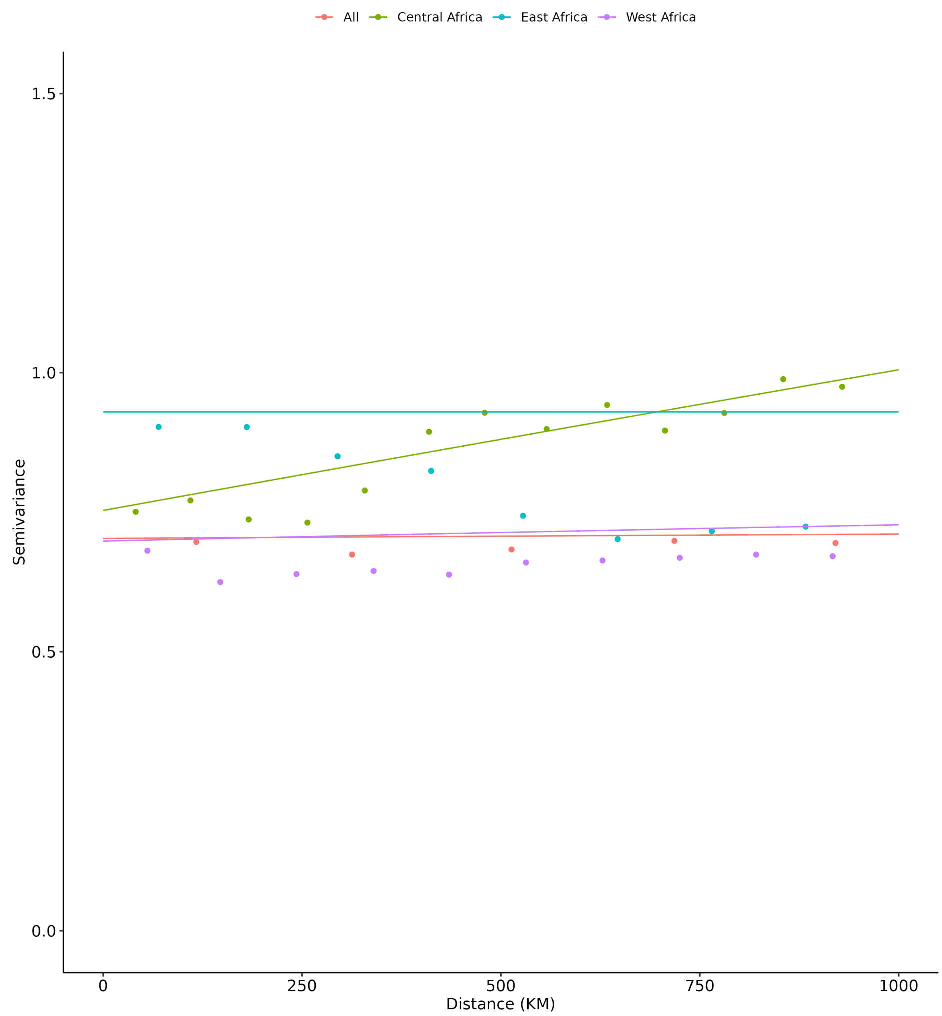

Figure 9: Semivariogram of residuals, grouped by observation region.

literature review, a collection of N=7,288 observations (ie approx. 15% of the training dataset, predominantly older data collected before mass scale-up of malaria control).

5.3 Model interpretation

Figures 12, 13, 14 show the derived relationships between the response and key predictor variables.

Figure 12 shows the three species-specific climate-malaria relationships as bivariate functions of HSI (x-axis) and TSI (y-axis), with lighter colours indicating higher contributions to the linear predictor (and therefore, all else equal, higher $Pf\mathrm{PR}_{2\text{-}10}$).

Figure 13 shows the nonlinear relationship between ITN coverage, pre-intervention *Pf*PR and ITN impact after 1 year. As in Bhatt *et al* [35], the parametric form of the relationship is based

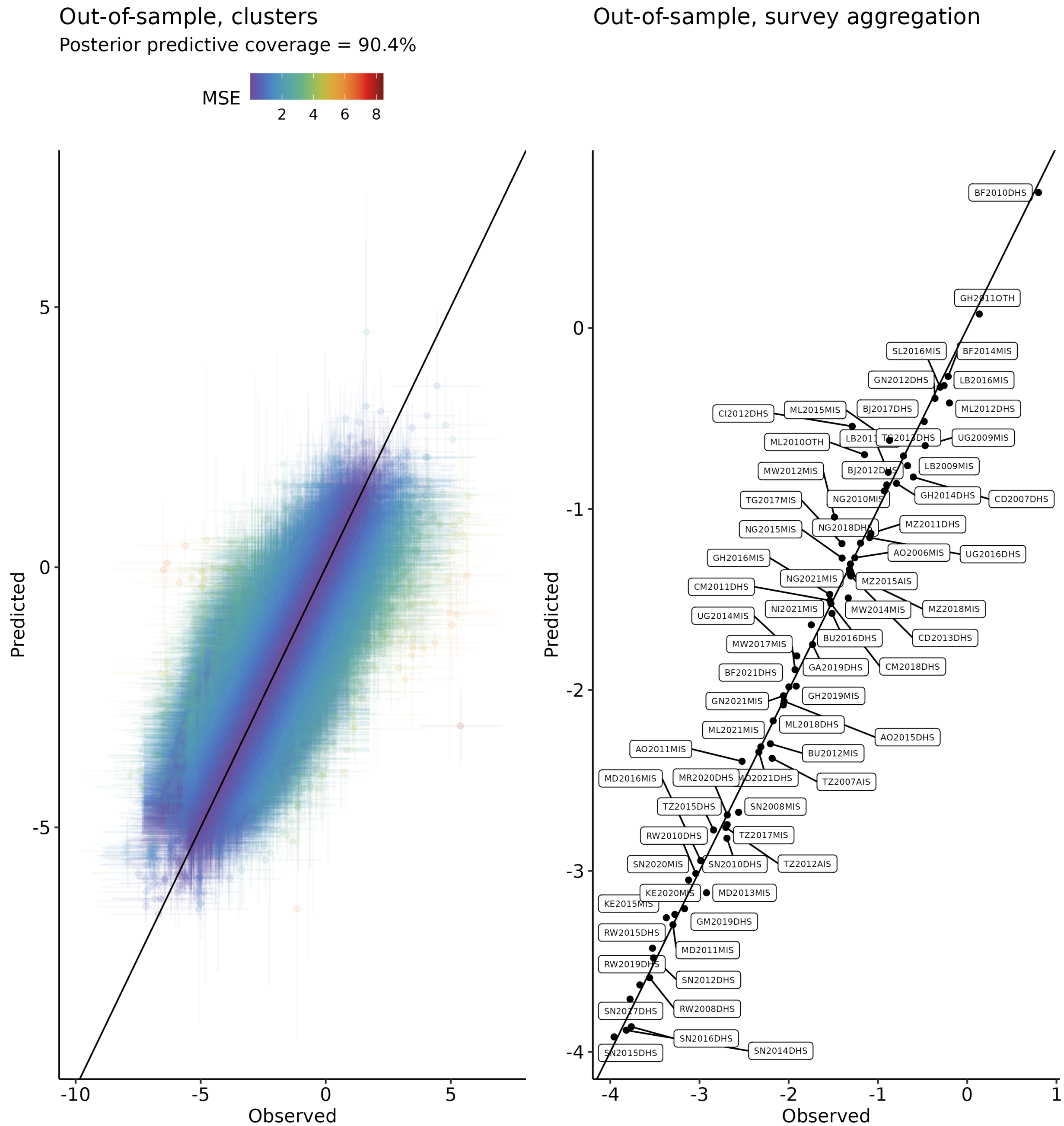

Figure 10: Out-of-sample model performance at (left) geo-located observation and (right) out-of-sample survey aggregate, respectively. Predictions reflect five-fold cross-validation, holding out 20% of the training dataset each fold (approx 10,000 clusters). Plots are presented in logit-space, reflecting the prediction targets of the model as fit. *Pf*PR$_{2\text{-}10}$-space statistics were: out-of-sample correlation (in *Pf*PR space) of 0.83, RMSE of 0.14, MAE of 0.10.

on simulations from OpenMalaria in order to model the dependency of ITN impact on both pre-intervention transmission and achieved coverage. The diagonal line (0% coverage) is shown in purple, before maximum impact is achieved at 100% coverage with saturation effects at extremely high and low *Pf*PR.

	MAE	RMSE	Coverage	Interval score
In-sample	0.09	0.09	92.1%	1.214
5-fold cross-validation	0.10	0.14	90.4%	1.394
Entire survey hold-out validation	0.12	0.19	90.2%	2.413

Table 6: **Model validation statistics.** Summary of final model performance (in *Pf*PR space), both in-sample and across two different forms of out-of-sample validation. Metrics are mean absolute error (MAE); root mean square error (RMSE); 95% posterior predictive coverage (ie proportion of observations falling within 95% posterior predicted intervals); and interval score, which additionally penalises wide uncertainty [49].

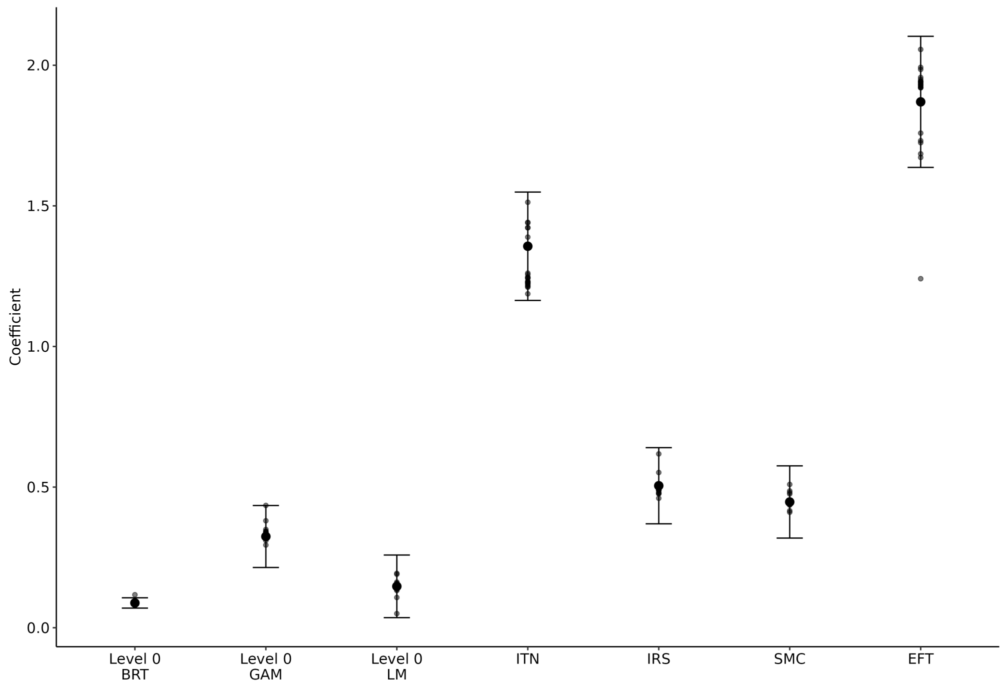

Figure 11: Sensitivity of Level 1 model fixed effect coefficients to 5-fold cross-validation and entire survey-held-out cross-validation. Error bars show the 95% CI of the Level 1 model coefficients with no data held out.

Figure 14 shows the relationship between treatment coverage and relative reduction in *Pf*PR. At lower levels of transmission, a given level of (population-level) access to effective treatment for clinical malaria was estimated to produce a greater relative reduction in *Pf*PR, compared to the same level of access in higher-transmission settings.

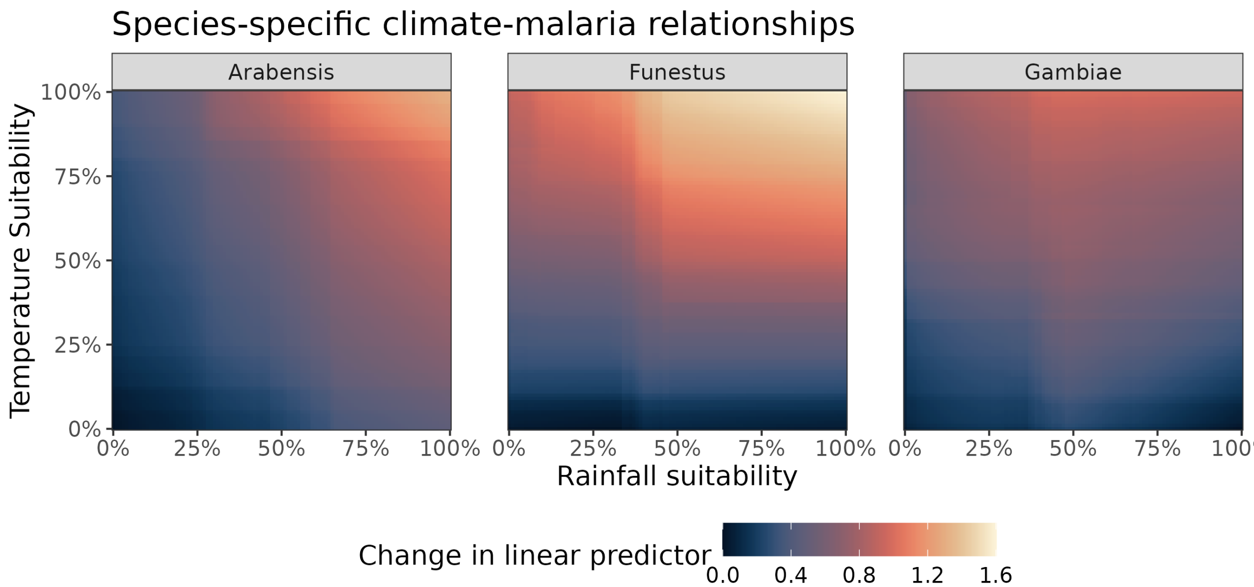

Figure 12: Learned change in contribution to linear predictor with varying TSI and HSI, by species. Change is relative to (0,0) intercept, so higher values indicate a larger linear predictor and higher *Pf*PR.

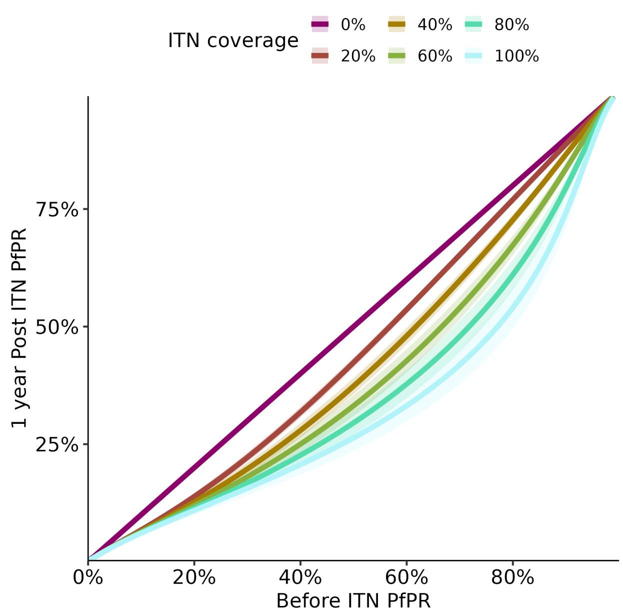

Figure 13: Expected reduction in PfPR as a function of intrinsic transmission (x-axis) and coverage with ITNs (colours).

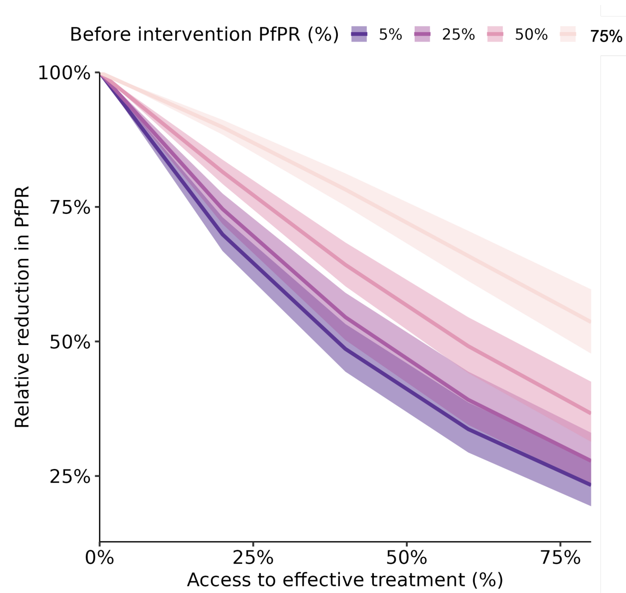

Figure 14: Relative reduction in PfPR as access to effective antimalarial treatment increases, as a function of pre-intervention/ITN PfPR. We find that, per unit increase of coverage, greater gains are achievable in lower-endemic settings.

6 Generation of future scenarios of extreme weather events

We projected flood and cyclone events separately through 2050. For both floods and cyclones, we created a backward event catalogue and projected future events based on these historic catalogues. For both floods and cyclones, we create forward scenarios for three GCMs (ACCESS-CM2, EC-Earth3-Veg-LR and MPI-ESM1-2-LR).

6.1 Summary of IPCC AR6 evidence base on extreme weather in Africa

To place into context our derived flood and cyclone scenarios, here we briefly summarise the IPCC AR6 Physical Science Report [50] and Impacts Adaptation and Vulnerability (Chapter 9: Africa) [51] findings on extreme weather events in Africa.

6.1.1 Flooding

Per IPCC AR6, fluvial flooding is projected to increase, with moderate confidence, in Central Africa. Heavy rainfall and pluvial flooding is projected to increase- with high confidence - in all regions of Africa except west South Africa (Namibia, western South Africa) [50, 51].

6.1.2 Tropical Cyclones

In the Indian Ocean cyclone track of southeast Africa and Madagascar, IPCC AR6 projects, with moderate confidence, a decrease in frequency, but increase in average tropical cyclone wind speeds, associated heavy precipitation and proportion of category 4 and 5 tropical cyclones [50, 51].

6.2 Scenario-based projections of flood events

Scenarios of area-days flooded 2024-2049 were constructed based on modelled flood frequency, duration and extent. Severity scores (1 and 2, as per DFO) were assigned according to area-days flooded. Relative importance of climate and geographical features in historical events was used to project the probability, duration and extent of flooding by month and water basin to 2050.

6.2.1 Historical flood data

Our training dataset consisted of 251 flood occurrence, extent and durations at the Level 4 Basin (defined based on Pfafstetter codes) level, extracted from Floodbase [13]. Floodbase uses a convolutional neural network based on MODIS satellite imagery at 230m resolution to identify flood events and assign attributes to them. Level 4 basins correspond to medium-sized sub-basins, from about 10,000 to 100,000 square kilometres in area. Floods occurring in the same L4 basin and month were joined into single events by duration (i.e., $\max(\text{start\_date}) - \min(\text{start\_date})$) and extent. Final model inputs were then unique L4 basin calendar month event occurrence, extent, and durations. These were linked to climate variables from the month of the given flood event (see Table 1). We included pluvial (surface) and fluvial (river) floods. Coastal floods were not considered in this analysis.

6.2.2 Modelling flood events

Four models were trained on the assumed historical flood data:

- Frequency: Likelihood of a flood occurring in a given basin in a given month
- Duration: Number of days of flooding event
- Extent: Number of km2 flooded in an event
- Areas: Grid cells flooded for each extent

Frequency

We used a random forest classifier on historic events (monthly flood events by L4 basin [n= 251]) to determine important features – see Table 7. Training data included historical flood events from the backward catalogue including relevant climate data by basin, topology and land cover. We also used the Fathom dataset in the forward catalogue to ascertain future flood risk by return period. Seventy percent of the data were used for training and 30% were used for the test dataset. We oversampled the training dataset due to data imbalance (an optimized rate of 3.7x flood events was selected using the Python package scikit-learn). Accuracy was calculated on the test dataset, which was a realistic (not oversampled) dataset. The AUC for the frequency model was 0.84, R2 for the duration model was 0.83 and R2 for the extent model was 0.81.

Feature	Lags	Importance
Rainfall	month -1, month, month +1	0.122
Average Atlantic Ocean sea-surface temperature	month -1, month, month +1	0.065
Average Indian Ocean sea-surface temperature	month -1, month, month +1	0.056
Location (latitude/longitude)		0.037
Month		0.019
Mean basin elevation		0.015
L3 basin		0.015
L4 basin		0.012
km of rivers within L4 basin		0.011
Area of L4 basin		0.010
% area above 1000m		0.010
% area covered by water bodies		0.010
Variance basin elevation		0.010
Average soil composition: sand		0.009
Average soil composition: clay		0.009
Variance soil composition: clay		0.009
Average soil composition: silt		0.009
Landcover: croplands		0.007
Landcover: urban and built-up		0.007
Landcover: barren		0.007
Variance soil composition: silt		0.007
Variance soil composition: sand		0.006
Area of lakes within L4 basin		0.005
Climate zone		0.005
Landcover: mixed forests		0.004
% area below 0m		0.003

Table 7: **Variables used in random forest classifier for flood occurrence**. Variables are sorted in describing order of variable importance. The prediction target was monthly flood events per L4 basin. Data was split 70/30 training/test, with oversampling of training data due to imbalance.

Extent and area

Extent within L4 basins was modelled using a random forest regressor, again with a 70/30 train-test split. Variables and importance are shown in Table 8. Test set R^2 was 0.83, RMSE was $3,400$km^2 (maximum flood extent was $120,000$km^2).

L4 basin estimates were then downscaled, with each grid-cell allocated a flood risk based on (70% weighting) frequency of historical floods and (30% weighting) Fathom [cite] risk scores. Cells within a flooded L4 basin were assigned to be flooded in descending order of risk until estimated extent was reached – see Figure 17, and Figure 18 for a visual comparison.

Total flooding is presented as km^2 days of flooding to account for frequency, duration and extent. Where flood extents were smaller than 25km^2, fractional extents were applied (and thus disruptions

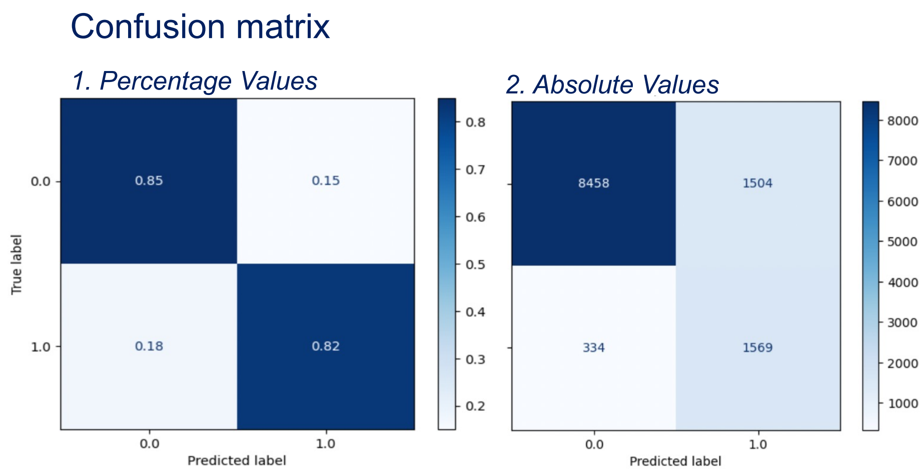

Figure 15: Out-of-sample confusion matrix for random forest classifier predictions of monthly flood occurrence at L4 basin level.

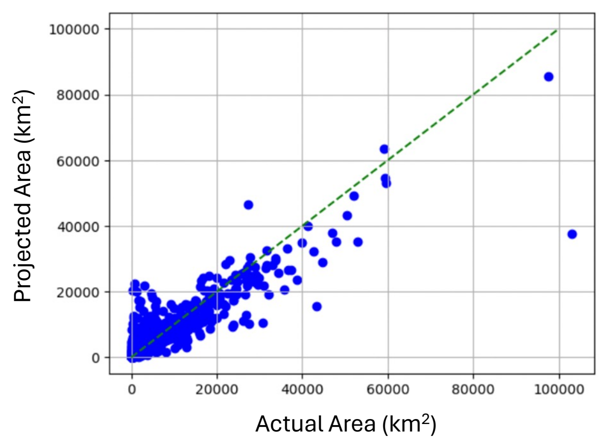

Figure 16: Out-of-sample validation of flood extent model, calculated on a 30% hold-out set.

were fractional downstream in the analysis).

Duration

A random forest regressor was fit to historical duration data, similar to the random forest models applied to extent and occurrence. Validated on a 30% hold-out test set, R^2 was 0.81, RMSE was 4.5 days and MAPE 35%. Table 9 shows the variables used and their fit importance.

Severity

Dartmouth Flood Observation classification of severity did not appear to be driven by total flood event size, duration or size-duration. Thus, severity cut-offs were defined based on the distribution of each class in historical flood :

- Top 48% of events by area-days flooded (corresponding to area-days $> 34,221$ km^2) classed

Feature	Lags	Importance
km of rivers within L4 basin		0.0102
Area of L4 basin		0.101
Rainfall	month -1, month, month +1	0.058
Average Atlantic Ocean sea-surface temperature	month -1, month, month +1	0.035
Average Indian Ocean sea-surface temperature	month -1, month, month +1	0.030
Area of lakes within L4 basin		0.030
Variance soil composition: sand		0.026
% area above 1000m		0.025
Variance soil composition: silt		0.024
Area of basin		0.023
Variance soil composition: clay		0.022
Location (latitude/longitude)		0.022
Landcover: croplands		0.018
Landcover: urban and built-up		0.017
% area covered by water bodies		0.016
Month		0.015
L4 basin		0.015
Variance basin elevation		0.014
Climate zone		0.012
Average soil composition: clay		0.012
L3 basin		0.009
Mean basin elevation		0.009
Landcover: mixed forests		0.009
Average soil composition: sand		0.007
Average soil composition: silt		0.007
% area below 0m		0.005

Table 8: **Variables used in random forest regressor for flood extent.** Variables are sorted in describing order of predicted variable importance. The prediction target was monthly flooded km^2 per L4 basin. Data was split 70/30 training/test, with oversampling of training data due to imbalance.

as severe flooding;

- Remaining 52% (area-days $\leq 34,221$ km^2) classed as moderate flooding.

Note that these severities were used only to determine disruption parameters applied as per Extended Data Table 3.

6.2.3 Creating projected flood scenarios

Per the extended methods, we calculated – for each downscaled and bias-corrected GCM M in our three-model ensemble – a future 'catalogue' of flood occurrence, duration and extent by L4 basin. To downscale the predicted L4 basin level extents, high-resolution occurrence data of

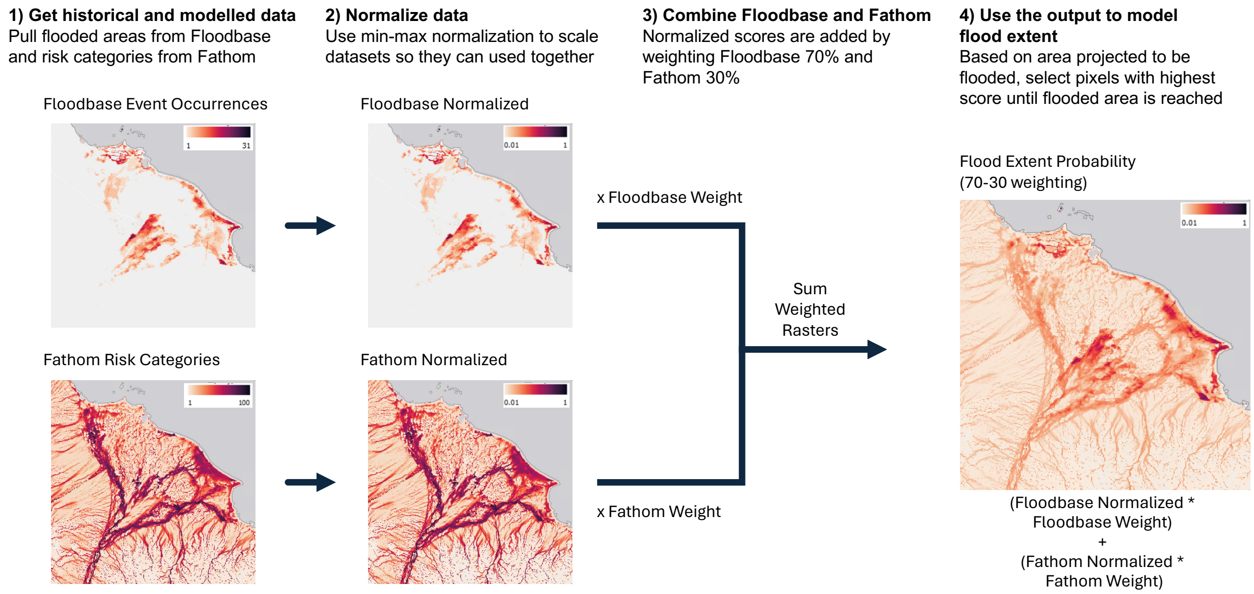

Figure 17: Overview of methodology used to downscale model flood extents to high-resolution flood area estimates. Tiles show processing of a representative flood event.

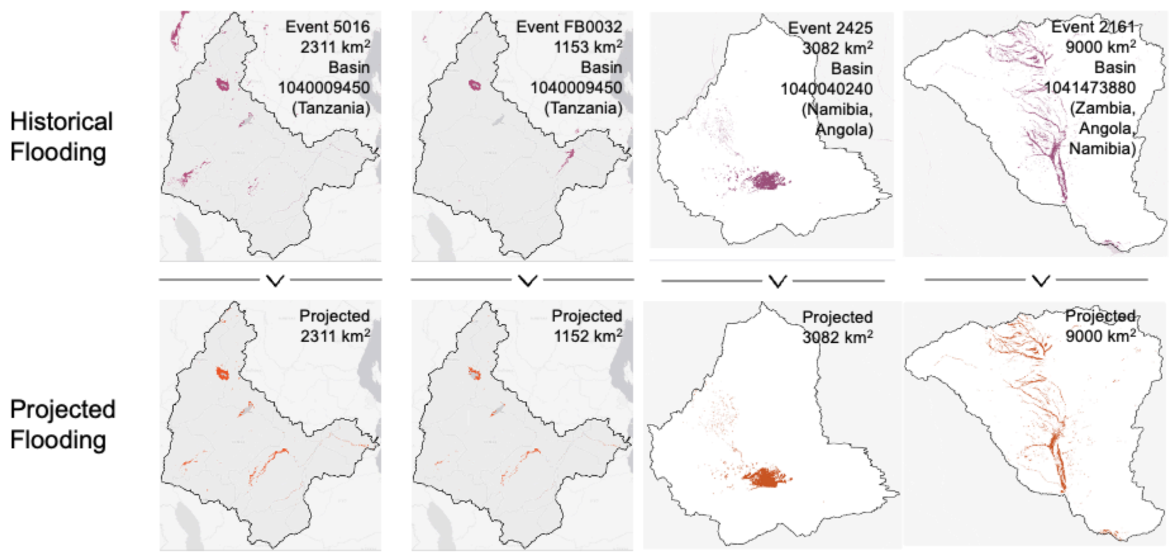

Figure 18: Visual validation of estimated flood areas compared to recorded historical events. Four flood events are plotted: in the top row the historical flood extent and on the second the model-based reconstruction of flood extent. Absolute values of flood extent for observed and predicted, respectively, are inset. Administrative boundaries were obtained from the Malaria Atlas Project [8].

historic floods were combined with a hydrological model and normalised to obtain, for each grid cell, within basin flood propensity scores. For each flood event within a basin, grid-cells were then flooded from highest to lowest flood propensity until predicted flood extent was reached. Projections were ceteris paribus, with land use variables held constant.

Feature	Lags	Importance
Average Indian Ocean sea-surface temperature	month -1, month, month +1	0.195
Average Atlantic Ocean sea-surface temperature	month -1, month, month +1	0.109
Location (latitude/longitude)		0.090
Rainfall	month -1, month, month +1	0.021
Mean basin elevation		0.019
L3 basin		0.014
Variance soil composition: clay		0.012
Landcover: croplands		0.011
Average soil composition: silt		0.011
Area of lakes within L4 basin		0.010
Landcover: barren		0.007
Landcover: mixed forests		0.007
Average soil composition: sand		0.007
Variance basin elevation		0.006
Month		0.005
Area of L4 basin		0.005
km of rivers within L4 basin		0.005
Landcover: urban and built-up		0.005
Average soil composition: clay		0.005
L4 basin		0.004
% area above 1000m		0.004
Variance soil composition: sand		0.004
Variance soil composition: silt		0.004
% area covered by water bodies		0.003
Climate zone		0.002
% area below 0m		0.001

Table 9: **Variables used in random forest regressor for flood duration.** Variables are sorted in descending order of predicted variable importance. The prediction target was days flooded per event per L4 basin. Data was split 70/30 training/test, with oversampling of training data due to imbalance.

For each GCM M and severity class s, a 'contemporary frequency' counterfactual scenario was simulated to provide a counterfactual for comparison with the corresponding SSP-245 projected scenario. First, the number of events $N_y^{M,s}$ in each simulated year y was sampled from a Poisson distribution with mean median$(N_{2024}^{M,s}, N_{2025}^{M,s}, N_{2026}^{M,s})$. $N_y^{M,s}$ events were then sampled from the 2024-2026 catalogues, thus constructing a forward scenario statistically resembling near-term ('contemporary') flooding frequency and extents. This was done for each GCM to minimise the impact of model bias in our climate-change-vs-counterfactual comparisons, as well as to replicate the stochastic spread of events inherent in the projected scenarios.

6.3 Scenario-based projections of cyclones

Historical cyclone data

We used IBTrACS (International Best Track Archive for Climate Stewardship) as a baseline of historic cyclone events, overlaid with CMIP6 global climate model data. We note the potential for missingdata in this dataset while recognizing its utility as the gold standard for historic cyclone cataloguing. We created a spatiotemporal backward catalogue (a shapefile) with the track of each historic cyclone and temporal features as lines. We classified cyclones from 1-5 using the Saffir-Simpson Hurricane Wind Scale. We then filtered for historic cyclones which made landfall or which were within 50km of the coast of Africa (n=192 from 1980-2024), based on the assumptions that only these cyclones which make landfall or which are close (≤ 50km) to the coast would be likely to drive meaningful malaria burden impact. Finally, we excluded extratropical cyclones due to their minimal impact on malaria burden.

Cyclones were assumed to begin at LMI, and tracks were terminated when modelled wind speed fell below tropical storm threshold (63 km/h). A counterfactual future scenario of cyclones reflecting present-day climate conditions was generated by resampling past cyclones, with Poisson rates of each category given by their frequency since 1980. Impact footprints were calculated based on R18, the radius of damaging winds.

Forward scenarios

The forward catalogue models spatial extent per projected cyclone and temporal track and features of projected cyclones separately, based on recent research using the Imperial College Storm Model (IRIS) Datasets. (31) We first modeled the spatial probability of LMI (Lifetime Maximum Intensity) locations and months for future cyclones making landfall in Africa. This is based on coordinates of past cyclones first observations and observance of Poisson's law (frequency and distribution has equal mean and variance). We then projected the cyclone track: for each LMI point, we projected synthetic tracks based on statistical correlation with climate drivers and past tracks. We finally projected the maximum sustained wind speed per projected event using statistical correlation with climate drivers. Only cyclones with landfall and with wind of at least a Category 1 wind speed on the Saffir-Simpson Hurricane Wind Scale are included in the forward catalogue. Modeling begins at the LMI; time steps before LMI are excluded. Decaying tropical cyclone tracks are terminated at the point at which wind speed falls below the tropical depression threshold. Notably, basins are simulated independently, so any inter-basin dependence is not present in the forward catalogue. Given the choice to limit tropical cyclones to at least Category 1 wind speed, the model will underestimate damage slightly: in the past 20 years, 14 tropical storms below Category 1 wind speed have occurred, of which four have caused material damage or displacement.

7 Parameterising impact of extreme weather events on housing and interventions

7.1 Literature review

The search terms for the literature review are recorded in Table 10. The final extracted papers are listed in Extended Data Table 2 and in Table 11, together with qualitative and – where they exist – quantitative summaries. The rubric used to assess the consensus and confidence of studies, used define the Harvey balls displayed in Extended Data Figure 2 is shown in Figure 19.

Weather Shock Event	**Malaria Impact Factor**	**Search Terms**
Floods	Larval Habitat	“Malaria” AND “larval habitat” AND “flood” AND “Africa”
		“Malaria” AND “larval habitat” AND “destruction” AND “flood” AND “Africa”
Floods	Access to Healthcare	(“infrastructure” OR “road” OR “healthcare service” OR “impassable” OR “disaster”) AND “flood”” AND “Africa””
Floods	ITN Access	(“LLIN” OR “ITN” OR “net”) AND “flood”” AND “Africa””; Google search: “LLIN” usage after “flood” in “Africa”
Floods	Housing	(housing OR displacement) AND ””flood”” AND ””Africa”” AND ””malaria””
Floods	Housing	(“housing” OR “displacement”) AND “flood” AND “Africa”
Cyclones	Larval Habitat	“Malaria” AND (“hurricane” OR “storm” OR “cyclone”) AND “Africa’
Cyclones	Access to Healthcare	(“infrastructure” OR “road” OR “healthcare service” OR “impassable” OR “disaster”) AND “cyclone” AND “Africa”
Cyclones	ITN Access	(“LLIN” OR “ITN” OR “net”) AND “cyclone” AND “Africa”; Google search: “LLIN” usage after “cyclone” in “Africa”
Cyclones	Housing	(“housing” OR “displacement”) AND “cyclone” AND “Africa” AND “malaria”

Table 10: **Search terms used in the literature review**. Peer-reviewed and grey literature were searched using the above terms to assess quantity and consensus of evidence on extreme weather event impacts on malaria transmission and control in Africa

Dimension	High	Medium	Low
Quality of evidence			
Volume of available research	• **Significant body of literature** on causal pathway(s) or other associations between extreme weather event & malaria impact	• **Moderate amount of literature** on evidence of causal pathways(s) or other associations between extreme weather event & malaria impact	• **Limited evidence** on causal pathway(s) or other associations between extreme weather event & malaria impact
Level of consensus in findings	• **Strong, consistent conclusions** on causal pathway(s) or other associations between extreme weather event & malaria impact	• **Some consistent conclusions** on causal pathway(s) or other associations between extreme weather event & malaria impact, but with multiple emerging potential conclusions	• **Significant variability in conclusions** across literature on causal pathways(s) or other associations between extreme weather event & malaria impact
Robustness of findings	• **Multiple, highly robust findings** from peer-reviewed journals & other high-quality sources (incl. WHO, IPCC) of direct relevance to the specific associations between extreme weather event & malaria impact	• **Generally high-quality findings** from at least one peer-reviewed journal with minimum level of relevance to associations between extreme weather event & malaria impact	• **Limited peer-reviewed evidence** or only documented through non-peer reviewed sources (incl. news reports, etc.) with tangential relevance to associations between extreme weather event & malaria impact

Figure 19: Quality rubric for literature review of extreme weather disruptions. Studies were assessed qualitatively across each of the three metrics, before being assigned an aggregate score with justification, as displayed in Extended Data Table 2.

Malaria impact	Authors	ISO	DOI	Qualitative	Quantitative
Larval habitat	Dambach et al., 2009	BFA	doi:10.3402/gha.v2i0.2094	Satellite data identifies malaria risk post flood	N/A
Larval habitat	Fillinger & Lindsay, 2011	Africa	doi:10.1186/1475-2875-10-353	Laval source management efforts lose effectiveness during floods	N/A
Larval habitat	Majambere et al., 2010	GMB	doi:10.1016/j.jinf.2009.11.013	Larvicide not effective in areas with regular flooding	N/A
Larval habitat	Castro et al., 2010	TZA	doi:10.1371/journal.pone.0010568	Clogged drains from floods increase larval habitat	N/A
Larval habitat	Chirebvu & Chimbari, 2015	BWA	doi:10.1111/jvec.12141	Flooding contributes to larval breeding	N/A
Access to Health-care	Petricola et al., 2022	MOZ	doi:10.1186/s12942-022-00315-2	Road network disruptions key	0.6-1.03M people lost access post Idai

Larval habitat	Thomson et al., 2017	Africa	doi:10.4269/ajtmh.16-0696	Climate & rainfall directly linked to malaria	N/A
Multiple	Xu et al., 2024	UGA	doi:10.1093/infdis/jiad348	Disruption and endemicity linked	N/A
Access to Healthcare	Mroz et al 2023	ZMB	doi:10.1186/s12942-023-00338-3	Reduced walking access to HC facilities	20% reduction in walking access
Access to Healthcare	Codjoe et al 2020	GHA	doi:10.1016/j.socscimed.2020.113072	Flooding disrupts community access to care	N/A
Access to Healthcare	Hierink et al., 2020	MOZ	doi:10.1136/bmjopen-2020-039138	Reduced travel speeds, barriers to movement, non-functional health facilities	~ 20% decrease in accessibility to care
Access to Healthcare	Adriano et al., 2023	MWI	doi:10.1097/MS9.0000000000000961	Disrupted service availability, rise in costs	83 healthcare facilities damaged/destroyed
Multiple	Mbunge et al., 2021	ZWE	doi:10.1016/j.puhip.2021.100168	LLIN distribution disrupted	N/A
Multiple	Mugabe et al., 2021	MOZ	doi:10.1136/bmjgh-2021-006778	ITN campaign post cyclone but still saw an increase in malaria positivity; delayed IRS campaign	More than 100 health facilities damaged
Housing	Kondo et al., 2002	MOZ	doi:10.1017/s1049023x00000340	Temporary housing conditions are poor	85% of patients post flood had an infectious disease; 1.5-2x increase in malaria cases
Housing	Salami et al., 2017	Africa	doi:10.1186/s12889-018-5687-1	Informal settlements more exposed to flooding & damage	N/A

Other	Lindblade et al., 2000	UGA	doi:10.1046/j.1365-3156.2000.00551.x	Farming in highland areas increased temp after replacing natural swamp vegetation with ag. Crops	N/A
Other	Bangs & Subianto, 1999	IDN	pubmed.ncbi.nlm.nih.gov/10928348/	Drought impact on malaria (both directly and as a second order impact of demographic movement	N/A
Other	Balikuddembe et al., 2023	East Africa	doi:10.1186/s41256-023-00294-0	Flood interacts with population displacement, overcrowding, sanitation issuest	N/A
Housing	Kelly-Hope et al., 2023	Africa	doi:10.1136/bmjgh-2023-012345	Floods lead to displacement	NA
Multiple	Alliance for Malaria Prevention, 2022	MOZ	allianceformalariaprevention.com/wp-content/uploads/2022/12/CaseStudy_Mozambique		500k ITNs distributed post Idai
ITN Access	Boyce et al., 2022	UGA	doi:10.1093/cid/ciab781		3 month delay to ITN campaign
Multiple	Searle et al., 2023	MOZ	doi:10.1038/s41598-023-45678-9	Lower ITN usage in houses with damage	59% HH report damage. RDT prevalence post cyclone = 31% (36% with house damage, 44% with destruction), 9 months on from Cyclone Idai, 64% people still living with household damage
Housing	WHO, 2019	MOZ	national-situation-report-1-10-may	Cyclones drive people to shelters with limited services	N/A

Multiple	Boyce et al., 2016	UGA	doi:10.1093/infdis/jiw363	Increased risk of positive RDT	30% increase in risk of positive RDT post-flood in villages bordering a flood-affected river
Larval habitat	Jambou et al., 2022	Sahel	hdoi:10.3390/ijerph191610105	Effect of flooding in raining season causing extended periods of malaria transmission	Range annual EIR 20-250
Larval habitat	Imbahale et al., 2011	KEN	doi:10.1186/1475-2875-10-81		86% of all habitats were as a result of human activities
Road	AfCAP, 2018	GHA	Adaptation in Ghana	Limited quantitative historical documentation	Severe floods in 2007: 332,600 people affected
Larval habitat	Vanhuysse et al., 2023	SEN	doi:10.1186/s12936-023-04527-0	Breeding sites abundant during the rainy season in flooded abandoned houses	
Other	Shu et al., 2023		doi:10.1038/s41467-023-43493-8	Flood exposure linked to population migration	
Housing	Charchuk et al., 2016	DRC	doi:10.1186/s12936-016-1479-z	Higher malaria burden in IDP camps than nearby villages	
Larval habitat	Messenger et al., 2023		doi:10.1016/S2214-109X(23)00044-X	Meta analysis on vector control strategies	

Table 11: **Literature review of disruptive impacts of weather on malaria**. Table summarises qualitative and quantitative interpretations of listed studies, expanding on Extended Data Table 2.

7.2 Expert interviews

Thirty-four expert stakeholders were interviewed. These included 11 climate scientists, 10 malaria scientists and policymakers living and working in the malaria-endemic studies included in this analysis, and 14 senior experts from international organisations which support the design, targeting, procurement and distribution of malaria control (including the Global Fund Against AIDS, Tuberculosis and Malaria, and the President's Malaria Initiative).

We selected these individuals purposively based on their positions in climate science, malaria and global health fields. We sought to collect a broad range of stakeholders across the academic, governmental and non-governmental spaces, focusing on stakeholders actively involved in similar work in the respective fields to gauge the state of the science and the diversity of current research and policy activities. We conducted semi-structured phone- or video-based interviews with all stakeholders based on an initial pool of pre-defined questions (Table 12).

Type of Stakeholder	**Questions**
Policy or high-level implementation	From your experiences, what are the key impacts on malaria after an extreme weather event like a flood or cyclone?
	What weather events have been most impactful to malaria programming in Sub-Saharan Africa?
	What aspects of service delivery are impacted the most? For how long were these elements of implementation disrupted during/after the weather events?
	At what point are services restored after the weather event?
	Were there any malaria-integrated emergency responses in light of an observed extreme weather event?
	What infrastructure issues (physical infrastructure, data systems, supply chains) are most common after extreme weather events? At what point after the weather event are these services restored?
	Are there discussions on climate & malaria in your organization? What is the general nature of these?
	Do you expect malaria implementation strategy to change in light of more frequent extreme weather events?
Local implementation	What share (%) of people were displaced from their homes while the flooding occurred?
	When people's homes were not damaged, did they return home as soon as flood waters receded?
	What share (%) of people's homes were damaged by the flood?
	What factors caused significant variation? (e.g., rural vs. urban, building materials, other?)
	For homes that were damaged, how long was it before families had a similar quality of housing again? (e.g., their home was repaired, a new home was built)
	How did active flooding impact roads and bridges, and therefore peoples' access to healthcare?

	Once flood waters receded, how much damage did roads and bridges sustain? How long before it was repaired to its prior quality (if ever)?
	Approximately what share (%) of healthcare facilities were damaged in a way that impacted their ability to provide ACT/RDT?
	How long did it take for local health facilities to be repaired (i.e., excluding any healthcare services provided in direct response to the flood)?
	To what extent did supply chain issues further affect service delivery (facilities which were operational but had stockouts)?
	To what extent are people covered by iCCM (integrated community case management of malaria) & to what extent was this affected?
	To what extent are RDTs, ACT available in IDP or other temporary housing settings?
	How was access to ITNs impacted by the flood event (e.g., lost, damaged)?
	While we know there are often nets distributed during the humanitarian response, did the shock delay a 'planned' campaign in any way? How long was it before a 'regular' campaign was run again?

Table 12: **Question scripts for semi-structured expert interviews.**

Transcripts of these interviews were recorded, and the key conclusions summarised in Extended Data Figure 3.

8 Projecting impact of extreme weather events on housing and interventions

8.1 Disruptions to interventions and access to improved housing caused by extreme weather

Extreme weather events were modelled as disrupting the above described interventions: access to ITNs, access to improved housing, and transport infrastructure determining accessibility to healthcare for clinical malaria. The magnitude and duration of disruption was parameterised for each event class and severity based on a mixed methods approach: a literature review extracted 17 studies from the peer-reviewed and grey literature discussing the impact of extreme weather events on the three considered drivers. This process was augmented with 35 expert interviews summarised in Extended Data Table 1. Note that these parameters represent unmitigated extreme events.

Parameters derived from this exercise were used to define recovery curves to be applied within geographic footprints of extreme events, as shown schematically in Extended Data Figure 2, with consensus parameters described in Extended Data Table 2. Acute and lasting impacts were differentiated, with the latter parameterised sigmoidally with parameters for time to 50% recovery and time to 99% recovery.

8.2 Disruptions to healthcare accessibility

As described in the main text, baseline access to effective treatment (EFT) for clinical malaria at location s was estimated using a composite of three surfaces obtained from the Malaria Atlas Project[8]: probability of care-seeking c_s; diagnosis and prescription of antimalarial drugs p_s^{drug}; and drug- and location- specific therapeutic efficacy (i.e. the probability of sustained clearance of parasitaemia within 28 days) E_s^{drug}:

$$\text{EFT}_s = c_s \sum_{\text{drug}} p_s^{\text{drug}} E_s^{\text{drug}}, \tag{26}$$

where drug can be one of Artemisinin Combination Therapy (ACT, the first-line treatment for falciparum malaria in Africa), Amodiaquine, SP, Chloroquine or quinine.

Using an established database of health facility geolocations[22], we determined baseline (disruption free) travel time to health facilities for each grid cell. A bi-exponential relationship between these travel times τ_s and geo-located observations of propensity to seek care for fever was fitted, resulting in the function:

$$t_{\text{decay}}(\tau_s) = 0.1451 \exp(-0.0798\tau_s) + 0.5396 \exp(-0.0008\tau_s). \tag{27}$$

Health facilities located within extreme weather extents were considered non-functional during acute impacts, with the proportion of facilities in each 5kmx5km grid cell remaining non-functional in the post-acute period sampled from a binomial distribution, with probability of closure given by intersecting the appropriate recovery curve with a time-since-last-event surface.

In addition to facility closures, damage to road infrastructure was parameterised as travel time penalties derived from the recovery curves and time-since-event surfaces overlaid on the OpenStreetMap road network [23]. Off-road travel time was recalculated by perturbing an established friction surface [22] in the same way.

8.2.1 Travel time to health facilities disruption

Given a graph of the road network, where nodes represent intersections and the weight for each edge is the time to travel the length of the street that connects them and a certain travel time threshold (e.g. 8h) we produced travel time to the closest functional health facility for each node and edge in the road network. The algorithm used was as follows:

1. Initialise a Map data structure to store nodes and their corresponding travel times to the closest health facility.
2. For each health facility location
   (a) Snap the location to a node in the graph
   (b) Use a specialised shortest path tree algorithm to find reachable areas within certain travel time limits (here set to 8 hours). The algorithm explores the graph in the reverse direction. Edges are traversed from their target back to their source nodes. Turn restrictions and weights are calculated in the reverse direction. This is particularly useful for creating reverse areas from which you can reach a health facility within a certain travel time threshold.
   (c) Update travel times for nodes, keeping the shortest travel time when multiple reachable facilities exist.
3. Given a distance threshold:
   (a) For each edge greater than the distance threshold
   (b) Split edge into smaller pieces.
   (c) For each resulting node:
      i. Calculates travel time using the information from the Map data structure, distance to the node, and travel speed.
      ii. Add travel times for nodes to Map data structure
4. Using a grid of cells, calculate the mean travel time of all the nodes within the cell.
5. Given a friction surface indicating the time to cross a cell, use the in Step 4:

(a) Calculate the travel time across the grid using a path find algorithm for those cells without travel times from Step 4.

8.2.2 Disruptions to access to effective antimalarial treatment

The result was monthly time to functional health facility surfaces, at 5kmx5km resolution, for each scenario (including counterfactual extreme weather event frequency). The above-described care-seeking relationship was then applied to these to calculate care-seeking penalties relative to baseline in the EFT equation, so that at time t and location s

$$\text{EFT}^{\text{scenario}}_{(s,t)} = \frac{t_{\text{decay}}(\tau^{\text{scenario}}_{s,t})}{t_{\text{decay}}(\tau^{\text{no disruption}}_{s})} c_s \sum_{\text{drug}} p^{\text{drug}}_s E^{\text{drug}}_s. \tag{28}$$

Antimalarial drug efficacy, proportional usage of different antimalarials, and secular spatial variation in care-seeking behaviour were held constant throughout.

8.3 Disruptions to ITN coverage

ITN campaigns were simulated continent-wide every three years on January 1st, commencing in 2022. As we aimed to model unmitigated impacts of extreme weather events, disrupted ITN coverage did not return to baseline until the next simulated campaign date. ITN access was assumed to be lost if access to housing was acutely disrupted.

8.4 Access to improved housing

Access to improved housing was directly perturbed from baseline values using the derived recovery curve.

8.5 Other interventions

SMC and IRS were not perturbed by extreme weather events due to a very limited existing evidence base on disruption by extreme weather. IRS – which is highly targeted, with only 2.35% of households in malaria-endemic Africa protected in 2022 – coverage was therefore held constant at 2022 levels in all scenarios, whilst SMC – as an age-targeted intervention with low-evidenced impact on transmission – was treated as a nuisance parameter when model fitting and held out of predicted $Pf\mathrm{PR}_{2\text{-}10}$. It is important to note that – even simply by a common sense assessment of their modes of distribution – both IRS and SMC campaigns are as vulnerable to disruption as ITN campaigns, so their absence from this analysis represents an absence of evidence rather than an absence of impact. Our projections are therefore conservative.

8.6 Baseline intervention summaries

Figure 20 shows baseline (unperturbed by extreme weather) ITN interaction and access to effective antimalarial treatment estimates used as baselines in this analysis.

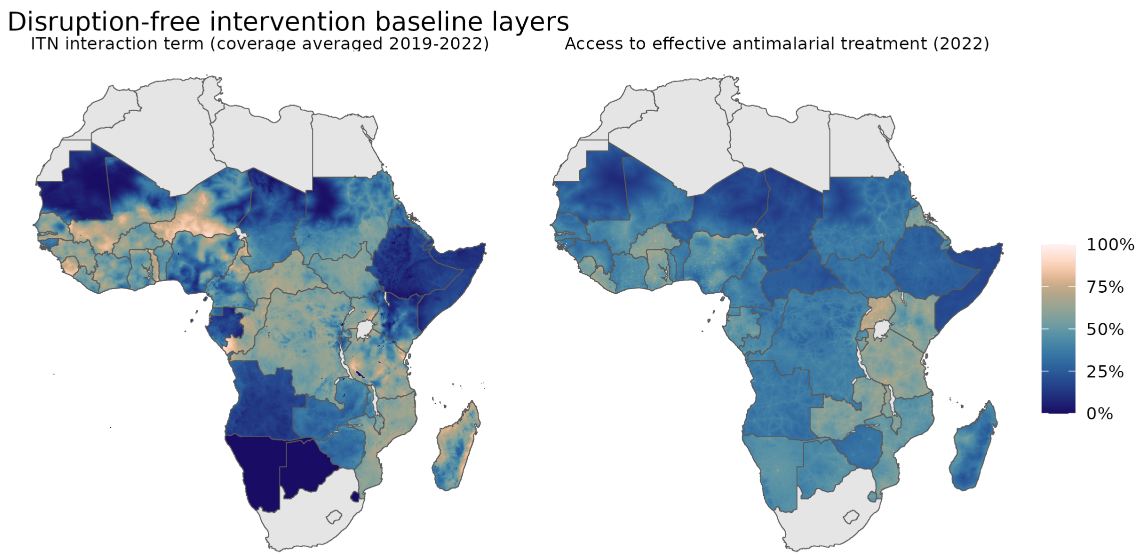

Figure 20: Baseline estimated surfaces of the ITN interaction term $\mathcal{I}$ and access to effective antimalarial treatment (untransformed) used in this analysis. These were used as baselines, which were perturbed by disruptions associated with extreme weather events as described in the methods. Administrative boundaries were obtained from the Malaria Atlas Project [8].

9 Projecting ecological and disruptive effects of climate change

A set of scenarios was defined to derive the (a) ecological; (b) disruptive; and (c) combined impacts of climate change by the 2040s. These are described in Extended Data Table 1 and described in the Extended Methods. Our assumptions about intervention coverages are described in detail above and in the main text. Permanent habitat, IRS and SMC coverage, and the posterior mean random field (capturing variation in *Pf*PR$_{2\text{-}10}$ not explained by the environmental, socio-economic, and malaria control factors explored in this analysis) were held constant. This allowed us to isolate the impact of our variables of interest.

For consistency and comparability, projections of *Pf*PR$_{2\text{-}10}$were differenced against a reference year (here 2022), with this delta applied to corresponding 2022 PfPR2-10 derived from observed (rather than modelled) climate data. Projected *Pf*PR$_{2\text{-}10}$ for each scenario was converted to clinical case incidence using an established natural history model [52]. Gridded population projections consistent with SSP 2-4.5 were used to generate estimates of absolute cases [24]. Projected time-series of clinical cases and mortality were scaled to align with 2022 official World Health Organisation estimates, as reported in World Malaria Report 2023 [36].

9.1 Calculating model consensus

The maps presented in Figures 1, 2 and 3 of the Main Text feature a bivariate legend, in which projected change in *Pf*PR$_{2\text{-}10}$(alternatively cumulative change in case incidence, for Fig. 3) is masked by 'model consensus'. This was calculated as follows:

1. Create – for each layer to be summarised – a sign raster s whose cell values are +1 if change is positive, -1 if negative.

2. Compute the absolute value of the sum the sign raster, $|\sum s| = S$, denoted S_{14} for 14-model ecological ensemble and S_3 for the reduced disruptive and combined effects ensemble. A score of 0 represents perfect disagreement (half ensemble positive, half negative change), whilst $S_3 = 3$ and $S_{14} = 14$ indicates perfect agreement on direction of change. Assign a consensus score:

$$s_{\text{score}} = \begin{cases} 1 & S_{14} \geq 10, S_3 = 3, \\ 0.75 & S_{14} \geq 7, S_{14} < 10, S_3 = 2, \\ 0.5 & S_{14} \geq 2, S_{14} < 7, S_3 = 1, \\ 0.25 & S_{14} \geq 1, S_3 = 0. \end{cases}$$

3. Calculate 5 x 5 km grid cell level summary statistic m (median, in the case of the time-averaged projections in shown in Figs 1,2,3), standard deviation σ.

4. Calculate the absolute coefficient of variation $\log(\sigma/|m|) =: c$. A lower c indicates higher ensemble agreement. Thus, assign

$$c_{\text{score}} = \begin{cases} 1 & c \leq 0, \\ 0.75 & c > 0, c \leq 2, \\ 0.5 & c > 2, c \leq 5, \\ 0.25 & c > 5. \end{cases}$$

Where $|m|$ is zero (i.e. the ensemble perfectly agrees on zero change) and therefore $c = \infty$, we set $c_{\text{score}} = 1$.

5. Calculate $a = \text{mean}(s_{\text{score}}, c_{\text{score}})$ and assign final score

$$\text{score} = \begin{cases} 1 & a = 1, \\ 0.75 & a \geq 0.67, a < 1, \\ 0.5 & a \geq 0.33, a < 0.67, \\ 0.25 & a \leq 0.33. \end{cases}$$

6. This score is used to determine transparency of final plot, with 1 indicating total opacity. The thresholds were scoring were chosen by visual assessment.

Mapped scores for Main Text Figures 1 and 2 are shown in Figure 21. There was high consensus on temperature suitability impacts, but less agreement on the impact of changing habitat suitability. This reflects greater between-GCM variation in both the magnitude and direction of projected rainfall changes relative to temperature. In general, the magnitude of individual GCM-specific habitat suitability impacts was smaller than the corresponding temperature suitability impacts, and cases where some models suggested substantial changes in habitat suitability were offset by others indicating opposite responses(Extended Data Figure 3).

9.2 Sensitivity analysis

To extend the above notion of between-GCM consensus and assess the sensitivity of our results to (i) the specific GCM used to derive the extreme weather scenarios and (ii) our assumptions about

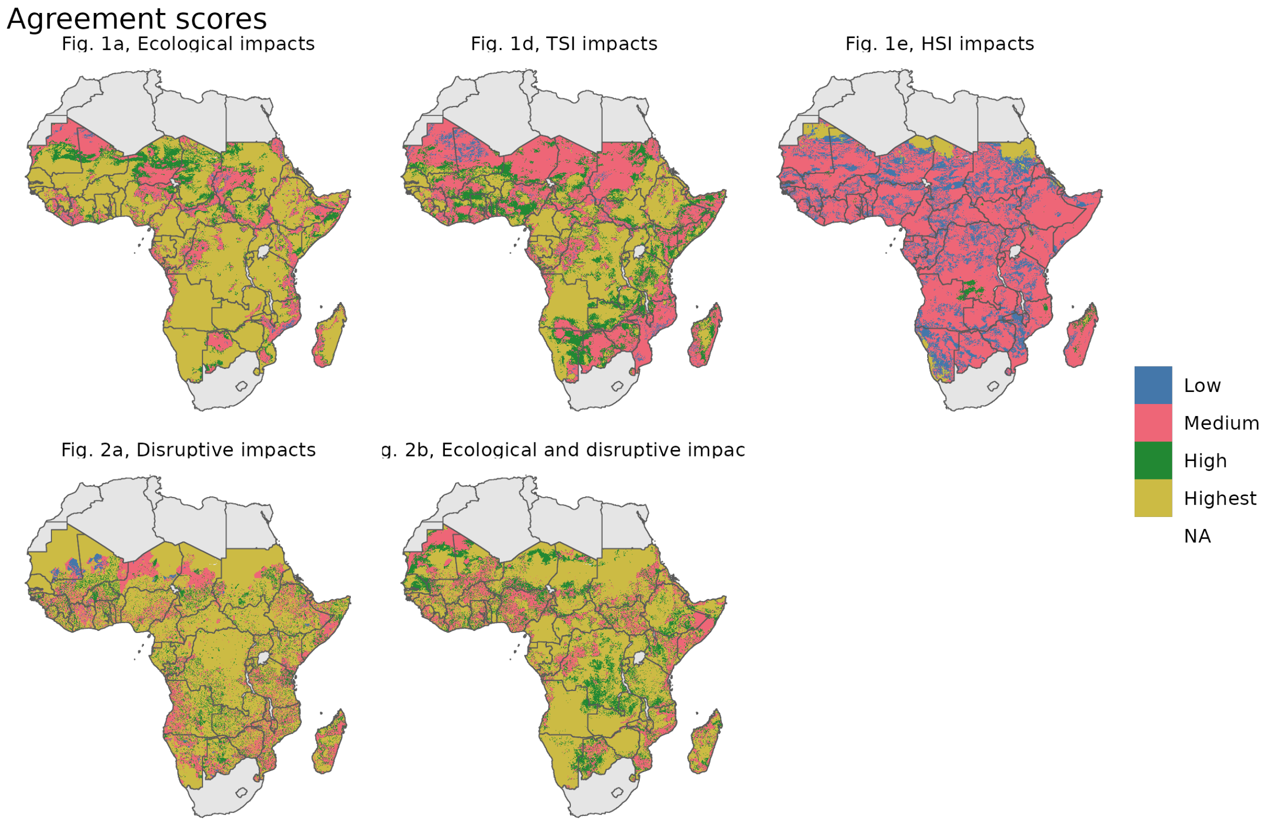

Figure 21: Model consensus scores used to mask opacity of Figures 1 and 2. Low (blue) corresponds to a score of 0.25, medium (pink) to 0.5, high (green) 0.75, and highest (yellow) to a score of 1. Administrative boundaries were obtained from the Malaria Atlas Project [8].

the magnitude of disruption following these events we ran – for each of the three GCMs – scenarios in which the magnitude of disruption to each of the three considered factors (improved housing, ITN coverage, and access to effective antimalarial treatment) was scaled by 50% and 150%. Each permutation of GCM model and impact factor scale was run. A summary of the results is presented in Extended Data Figure 5.

9.3 Computational note

This results in this paper were generated in R 4.2.1 [53]. The parameters of the geostatistical improved housing model were fit using greta v0.4.3.9 [54]. The malaria model was fit in R 4.2.0 using mgcv v1.8-40 [55], gbm v2.1.8.1 [56] and INLA v22.12.16 [57]. paws v0.7.0 [58] was used extensively throughout this analysis when interfacing with AWS.

Figures were generated using tidyverse v2.0.0, ggplot v2_3.5.1, terra v1.7.83, sf v1.0-18, tidyterra v0.6.1, ggpubr v0.6.0, ggtext v0.1.2 and ggridges v0.5.6.9000 [59–66]. Colour palettes from the khroma, scico, NatParksPalettes and viridis packages were used [67–70]. Palettes used to display continuous data are perceptually uniform. All are colour-blind safe.

The code used to generate the *Pf*$PR_{2\text{-}10}$ projections described in this paper is available at: `https://gitlab.com/tasminsymons/map-climatechangeimpacts`.

10 Overall summary of study

Table 13 summarises this modelling study, detailing for each element of Extended Data Figure 1 pre-existing research built on in this work, and the strengths and limitations of this study.

Component	Category	Pre-existing versus new elements	Strengths and limitations
1. Preparation of consistent geotemporal climatologies, 2000-2050			
High-res historical climate data (temperature, humidity, rainfall)	Input data	All historical climate data was sourced from pre-existing third-party products. See Table 1 for references.	These data were identified as best-in-class products, although are themselves the results of models applied to observational data of varying accuracy, completeness and sampling density. Accuracy will therefore vary spatially and temporally, although this is not accounted for and not propagated into downstream analysis steps.
Downscaled and bias-corrected CMIP6 outputs (temperature, humidity, rainfall)	Input data	All projected climate data were sourced from pre-existing third-party products. See Table 1 for references.	The CMIP6 ensemble reflects current state-of-the-art in climate modelling. Projections differ between individual climate models, reflecting natural stochasticity and structural uncertainty the climate system. Our use of multiple CMIP6 members allows assembling of our results, reducing reliance on a single climate model. CMIP6 projections are spatially coarse and not strictly consistent with historical observations, and so we use a downscaled and bias-corrected product. Resulting uncertainties are not propagated.
Additional downscale and calibration to historical data	Analysis step	New procedure developed for this study	Further in-house calibration and downscaling were required to achieve alignment with the particular choice of historical climate data used in this study. Any imprecision incurred in this process was not propagated into subsequent steps.
Geotemporal climate data	Intermediate output	New output generated in this study.	Modelled estimates/projections are at high spatial and temporal resolution, consistently link historical to projected values, and reflect projections from multiple CMIP6 member models. As described in preceding steps, multiple sources of imprecision and uncertainty are not propagated.

2. Modelling of historical and projected climate suitability indices			
Temperature suitability model	Analysis step	Preceding modelling by authors [27] was built on this study, including the incorporation of new third-party work on vector temperature dependence [71].	New suitability model captures current state-of-the-art on temperature dependent sporogony of Anopheles gambiae. Other important vectors not differentiated, and may have different dependency relationships. Temperature suitability model relies on gridded climatology data, and so does not account for micro-climatic variations for example mediating effects of vegetation or human structures.
Larval habitat suitability model	Analysis step	New modelling developed for this study. Incorporated previously defined mechanistic relationships [32].	Habitat suitability model captures limiting process of rainfall and subsequent evaporation in determining likely availability of surface water with adequate persistence for larval development. Accuracy dependent on fidelity of gridded climate data. Model does not capture influence of land cover or local hydrological processes.
Permanent larval habitat model	Analysis step	New modelling developed for this study.	Permanent habitat is differentiated from transitory habitat modelled in previous step, reflecting water bodies that are less dependent on local and variable rainfall, and that are detectable on satellite imagery. Smaller permanent habitats may not be captured.
Climate suitability indices 2000-2022; 2024-2050	Intermediate output	New output generated in this study resulting from above steps in this analysis stage.	Suitability indices were subject to the strengths and limitations described above.
3. Preparation of historical geotemporal housing, intervention and contextual data			
Population and GDP data (55km; 2000-2022)	Input data	Sourced from pre-existing third-party products. See Table 1 for references.	The gridded population data used were originally modelled based on census, survey, and other demographic data, and the fidelity of pixel-level values will vary with the quality of those sources. National-level GDP data are a standard way of assessing macro-level economic development, but it should only be interpreted as a crude proxy and often fails to represent trajectories of wealth and equity across the population. Uncertainty in GDP and population was not available and not propagated into subsequent modelling steps.
Survey observations of housing quality	Input data	Sourced from pre-existing third-party data. See Table 1 for references.	Housing data from nationally representative cross-sectional surveys provides a robust and comparable source of information on key attributes of housing quality and construction relevant to malaria risk. Data availability and recency varies considerably between countries.

Geotemporal housing model	Analysis step	Implementation of model previously developed by authors [72], with additional refinement for this study.	This model predicts the fraction of population living in an unimproved house which has previously been demonstrated as a strong driver of malaria risk. The model performs well in out-of-sample validation, with strong spatial autocorrelation and highly predictive covariates enabling relatively precise predictions at pixel level.
Improved housing	Intermediate output	Updated output generated in this study resulting from above steps in this analysis stage.	The predicted geotemporal housing layer has generally high accuracy but is subject to the limitations of the input covariate and response data as described above.
Treatment coverage	Input data	Sourced from pre-existing product modelled by authors. See Table 1 for references.	The MAP treatment coverage model combines survey data on care seeking behaviour and access to different antimalarial drugs, programmatic data on drug consumption, and data on drug resistance compiled from therapeutic efficacy studies. These data inputs vary greatly in their fidelity and abundance, and local precision of the modelled coverage inevitably varies accordingly. In particular, understanding of service access, proportional drug usage by type, and type-specific trends in non-ACT efficacy are not well measured in the years between 2000 and 2005.
Vector control coverage	Input data	Sourced from pre-existing product modelled by authors. See Table 1 for references.	The MAP ITN coverage model combines survey data on ITN ownership and usage with programmatic data on bednet procurement and distribution. The model performs well in out-of-sample validation, although uncertainty increases in periods and countries without recent national surveys. The MAP IRS model is less sophisticated and is driven primarily from programmatic records denoting the timing and coverage of spray campaigns. Declining efficacy of IRS post deployment is not explicitly modelled.
Relative vector abundance	Input data	Sourced from pre-existing product modelled by authors. See Table 1 for references.	Predictive maps of the relative density of the main African anopheles vectors of malaria were originally generated by MAP and more recently updated by the Vector Atlas Project. These represent the most comprehensive assembly of vector abundance data across Africa, and the predictive modelling performs strongly out-of-sample. Sparsity of data means variation in relative abundance over time is not captured, and other minor malaria vector species are not incorporated.
4. Preparation of historical malaria response data			

Literature and household survey observations of PfPR (N=50k, 2000-2022)	Input data	This MAP PfPR database was initiated in 2005 and is updated by the authors on an ongoing basis [8].	The MAP PfPR database is a near-exhaustive assembly of malaria infection prevalence data collected in Africa over the past 25 years, combing data from individual studies with systematic nationally representative household surveys. Data coverage varies considerably by country and through time, with earlier periods, in particular, having less consistent coverage.
Age standardisation model	Analysis step	Implementation of model previously developed by authors [41].	MAP has a long-established model that captures typical age structure of PfPR based on a large training dataset. Local variation in that relationship for example driven by locally varying demographic structure or age-specific exposure is not captured.
Diagnostic standardisation model	Analysis step	Implementation of model previously developed by authors [42]	MAP has developed a model to allow standardisation between PfPR observations captured via Rapid Diagnostic Test versus via blood smears read with light microscopy. The model is trained on a very large dataset of pairwise observations. While the model is highly predictive (reflecting the stability and consistency of this relationship) it does not necessarily capture local sources of variation nor changes to this relationship over time (driven for example by variable sensitivity and specificity of light microscopy from different laboratories and operators).
Standardised PfPR2-10 observations	Intermediate output	Updated output generated for this study.	The final set of age- and diagnostic-standardized PfPR used for this study reflects a uniquely valuable resource for quantifying trends in infection prevalence over time and between regions in Africa over the past 25 years. This forms the primary calibration data set in this study for characterizing the influence of climate on malaria. This finalised data set is subject to the strengths and limitations of the raw data and preparatory steps described above.
5. Characterising historical climate, housing, intervention and other contextual effects on malaria			

Space-time geostatistical model (including stacked generalisation step)	Analysis step	Development of a new framework that built on conceptual design conceived of previously by authors [35, 44], but with various elements refined and adapted for this study.	This new framework is more flexible than model-based geostatistical approaches used elsewhere: the stacked generalisation approach allows for flexible, non-linear response-predictor relationships whilst being robust to overfitting. Demonstrating this, the model performs well in out-of-sample validation, and (heuristically) reproduces the expected bio- and ecologically relationships between the response and predictor variables. Although the complexity of the model can lead to challenges of interpretation, deliberately simple choices of level 0 models (a linear model, GAM and BRT) and simple stacking (see REF) increase interpretability. In all cases, the model coefficients are global (both spatially and temporally), which may not be entirely realistic. However, interaction terms with spatially-varying abundance of key malaria vector species does introduce spatial variation in the climate-malaria relationship.
Parameterisation of climate, socioeconomic, intervention effects on PfPR	Intermediate output	New parametrisations characterising these relationships generated for this study.	These parameterizations are central to the findings of the study. By bringing together (via preceding analysis stages 1-4) detailed reconstructions of geotemporal information on malaria climatic suitability, malaria intervention coverages, and background socioeconomic conditions, and modelling how those factors explain variation in the large assembly of PfPR observations across Africa since the year 2000, we have sought to enable the most robust possible characterisation of these underlying relationships. As described in the numerous preceding steps, each component is subject to uncertainty, not all of which is formally propagated into the learned parametrisations (we do not, for example, account for errors-in-variables). However, to the extent the imperfections in covariate data leads to uncertainty in parameterisation, this is captured in the posterior distribution of each learned parameter.
6. Generation of future scenarios of extreme weather events			
Repositories of past extreme events (DFO, IBTrACS)	Input data	Sourced from pre-existing third-party data. See Table 1 for references.	The Dartmouth Flood Observatory provides a geospatial catalogue of recorded flood events, derived from news, governmental, instrumental, and remote sensing sources from 1985 to the present. While smaller and transitory flood events may be omitted, this resource is considered a relatively comprehensive archive of events. IBTrACS is a similarly comprehensive archive of tropical cyclone events and their location and intensity.

Present-day hydrological flood risk models (Fathom, FloodBase)	Input data	Sourced from pre-existing third-party data. See Table 1 for references.	The Fathom flood risk product provides very high-resolution descriptions of contemporary flood risk derived from detailed topographic and hydrological modelling. Likewise, FloodBase derives detailed historic flood extent maps based on high resolution satellite imagery. Both products are considered to have best-in-class levels of accuracy and offer robust flood risk delineation at the spatial resolution required for the present study. Triangulating both products allowed consensus flood extents to be identified in locations where the individual extent predictions differed.
Statistical models of flood and cyclone extents, duration and severity	Analysis step	New modelling developed for this study.	A new methodology was developed for this study to generate a catalogue of future floods (characterised by their spatial extent, severity, and duration) that was consistent with the climatological projections from GCMs. Simulation across multiple CMIP6 ensemble members captured a degree of between-model variation. The within-basin downscaling step heuristically applied knowledge of present-day local flood risk to refine simulated basin-level events and delineate predicted flood extents at pixel level. Future projection of both flood and cyclone events relies on a predictive model and assumes observed covariate relationships trained on past events and historical climate data are stable and predictive of future events.
Future scenarios of flooding and cyclone events	Intermediate output	New output generated for this study.	The basin-level predictive modelling steps for flood extent, severity and duration demonstrated satisfactory out-of-sample performance, as did the predictive model for future simulation of cyclone events consistent with GCM projections.
7. Parameterising impact of extreme weather events on housing/interventions			
Extreme weather events - literature review on measured impacts	Input data	Sourced from pre-existing third-party data in literature. See Table 1 for references.	This comprehensive and systematic literature review likely found all relevant published studies. These were relatively rare for African settings. It is likely that some additional useful information in uncatalogued, informal or grey literature was not identified. Identified studies contained rich information of extreme weather event impacts on malaria. This tended to be highly locally specific and often provided qualitative rather than quantitative metrics of impact.

Extreme weather events - stakeholder interviews on experienced impacts	Input data	New information collected from expert stakeholders as part of this study.	The stakeholder group had extensive and diverse expertise and first-hand experience of extreme weather events in Africa, their impact on malaria transmission and control, and longer-term impacts on health systems and infrastructure. Perspectives included nationally based personnel as well as those representing international aid, development, and health agencies.
Synthesis to identify main disruption pathways leading to malaria impact	Analysis step	New analysis for this study.	Condensing the rich accounts of stakeholders into standardised information for use in this study necessitated simplification and abstraction, and subjective judgements were sometimes required to capture information systematically. Not all locally specific experiences and nuances could be captured. However, there was strong consensus on the primary disruption pathways identified.
Synthesis into quantitative estimates of disruption type, magnitude and duration	Analysis step	New analysis for this study.	Only a subset of stakeholder and literature-derived information was adequately specific and quantitative to inform disruption measures, and there was considerable variability. This was addressed in the study by the use of large sensitivity ranges around each metric, which were then propagated into all downstream analyses.
Look-up table of event impact magnitude and duration by type, pathway, and severity	Intermediate output	New output generated for this study.	Estimated event impact parameters are subject to the strengths and limitations described above.
8. Projecting impact of extreme weather events on housing/interventions			
Integration of simulated events and event impact parameters to derive per-event impact on housing and interventions relative to present-day undisrupted	Analysis step	New analysis for this study.	Arithmetic combination of simulated event and event impact parameters to yield disrupted housing and intervention coverages. On a pixel-by-pixel basis, this assumes that the range of impacts associated with an event of a given type, magnitude, severity and duration is uniform across Africa and though time. The defined scenarios also hold (pre-disruption) housing and interventions constant at contemporary levels.

Vector control coverage, improved housing coverage, treatment coverage with extreme weather disruptions	Intermediate output	New output generated for this study.	Simulated disrupted coverages are subject to the strengths and limitations described of the upstream modelling components, with the largest source of uncertainty likely being the compiled event impact magnitudes. The large sensitivity ranges imposed on these impact parameterisations allow simulated disruptions to reflect this uncertainty and propagate it into subsequent modelling steps.
9. Projecting ecological and disruptive effects of climate change			
Space-time geostatistical model:	Analysis step	Development of a new framework that built on conceptual design conceived of previously by authors [35, 44], but with various elements refined and adapted for this study.	As mentioned in Stage 5, the central geostatistical architecture for PfPR prediction was validated extensively out-of-sample using a variety of different hold-out approaches to probe different elements of performance. This demonstrated both accuracy around point estimates and coverage performance of posterior credible intervals that was appropriate to support the aims of the study and the interpretations drawn.
PfPR 2024-2050	Final study output	New output generated for this study.	These forward projections of PfPR are contingent on the performance of the geostatistical model, discussed immediately above, as well as the numerous upstream assumptions, data inputs and modelling components comprising Stages 1-8. Modelled uncertainty captures many but not all sources of uncertainty and imprecision.
Natural history model for clinical incidence	Analysis step	Implementation of model previously developed by authors [52].	High-quality observations of malaria clinical incidence in the community are challenging to collect and studies reporting this type of data are rare. Mechanistic understanding of the processes governing the relationships between PfPR and clinical incidence rate is imperfect. Nonetheless, this model was fitted to a comprehensive dataset of community-observed malaria clinical incidence from Africa and use an ensemble of three leading mechanistic models to characterise this relationship, with structural as well as statistical uncertainty captured across the resulting ensembled fit.
Clinical incidence 2024-2050	Final study output	New output generated for this study.	These forward projections of clinical incidence rate are contingent on both the underlying PfPR prediction and subsequent modelled conversion to incidence, both discussed above. As with PfPR, modelled uncertainty in incidence rate captures many but not all sources of uncertainty and imprecision.

Scenario comparisons	Analysis step	New analysis for this study.	Scenarios were configured to allow projected climate change impacts to be identified separately for ecologically- and disruption-driven impacts, as well as both pathways combined. In all scenarios we assumed underlying socioeconomic conditions and baseline intervention coverages were as observed in the present day. This allowed climate change impacts to be inferred in isolation, but did not consider how other long-term non-climate trends may interact with climate change.
Impact of climate change on malaria	Final study output	New output generated for this study.	Our final estimates and conclusions on the potential impact of climate change on malaria have numerous strengths relative to preceding studies with the most important being: (i) the calibration of the relationships between climatic conditions and malaria risk using a very large historic database and while controlling for variation in a wide range of non-climatic factors that strongly influence malaria; and (ii) the consideration of not only ecological pathways but also the effect of damage and disruption to infrastructure and control efforts. The study also has a wide range of limitations and each of the many moving parts that comprise the modelling framework could in principle be strengthened as new data and approaches are developed. Like most climate change analyses, the findings are strongly contingent on the underlying CMIP6 member climate projections. Additional major sources of uncertainty specific to this study include the paucity of quantitative evidence on the magnitude of impact that extreme weather events excerpt on infrastructure and malaria control. We have attempted to mitigate for this uncertainty by combining both literature review data with stakeholder interviews, and to then compile and synthesise that evidence base with a sensitivity approach that imposed wide uncertainty ranges for downstream propagation. Other uncertainty stems from the need to generate simulated future flood and cyclone extents driven from the CMIP6 ensemble. While performing well in validation, such a modelling exercise is challenging and heavily contingent on the fidelity of input data. We also address only a subset of possible climate-driven impacts on malaria. Other extreme events such as coastal flooding and drought were not considered, nor were indirect mechanisms such as conflict, migration or macro-economic effects.

Table 13: **Summary of this modelling study.**

References

1. Weiss, D. J. *et al.* An effective approach for gap-filling continental scale remotely sensed time-series. *ISPRS J Photogramm Remote Sens* **98,** 106–118 (2014).
2. Weiss, D. J. *et al.* Re-examining environmental correlates of Plasmodium falciparum malaria endemicity: a data-intensive variable selection approach. *Malar J* **14,** 68 (2015).
3. Funk, C. *et al.* The climate hazards infrared precipitation with stationsa new environmental record for monitoring extremes. *Scientific data* **2,** 1–21 (2015).
4. Harris, I., Osborn, T. J., Jones, P. & Lister, D. Version 4 of the CRU TS monthly high-resolution gridded multivariate climate dataset. *Scientific data* **7,** 109 (2020).
5. Lobser, S. E. & Cohen, W. B. MODIS tasselled cap: land cover characteristics expressed through transformed MODIS data. *International Journal of Remote Sensing* **28,** 5079–5101 (2007).
6. Fick, S. E. & Hijmans, R. J. WorldClim 2: new 1-km spatial resolution climate surfaces for global land areas. *International journal of climatology* **37,** 4302–4315 (2017).
7. Zomer, R. J., Xu, J. & Trabucco, A. Version 3 of the global aridity index and potential evapotranspiration database. *Scientific Data* **9,** 409 (2022).
8. Malaria Atlas Project. *Malaria Atlas Project Data* 2025. `https://data.malariaatlas.org`.
9. Murakami, D., Yoshida, T. & Yamagata, Y. Gridded GDP projections compatible with the five SSPs (shared socioeconomic pathways). *Frontiers in Built Environment* **7,** 760306 (2021).
10. Lehner, B. & Grill, G. Global river hydrography and network routing: baseline data and new approaches to study the world's large river systems. *Hydrological Processes* **27,** 2171–2186 (2013).
11. Kottek, M., Grieser, J., Beck, C., Rudolf, B. & Rubel, F. World map of the Köppen-Geiger climate classification updated (2006).
12. Lehner, B., Verdin, K. & Jarvis, A. New global hydrography derived from spaceborne elevation data. *Eos, Transactions American Geophysical Union* **89,** 93–94 (2008).

13. Tellman, B. *et al.* Satellite imaging reveals increased proportion of population exposed to floods. *Nature* **596,** 80–86 (2021).

14. Friedl, M & Sulla-Menashe, D. *MODIS/Terra+ Aqua land cover type yearly L3 global 500m SIN grid V061 [Dataset]. NASA EOSDIS Land Processes DAAC* 2022.

15. Vermote, E., Justice, C., Claverie, M. & Franch, B. Preliminary analysis of the performance of the Landsat 8/OLI land surface reflectance product. *Remote sensing of environment* **185,** 46–56 (2016).

16. Batjes, N. H., Calisto, L. & de Sousa, L. M. Providing quality-assessed and standardised soil data to support global mapping and modelling (WoSIS snapshot 2023). *Earth System Science Data* **16,** 4735–4765 (2024).

17. For Environmental Information, N. N. C. *ETOPO 2022 15 arc-second global relief model* 2022.

18. Lehner, B. & Döll, P. Development and validation of a global database of lakes, reservoirs and wetlands. *Journal of hydrology* **296,** 1–22 (2004).

19. Knapp, K. R., Kruk, M. C., Levinson, D. H., Diamond, H. J. & Neumann, C. J. The international best track archive for climate stewardship (IBTrACS) unifying tropical cyclone data. *Bulletin of the American Meteorological Society* **91,** 363–376 (2010).

20. Hersbach, H. *et al. ERA5 hourly data on single levels from 1940 to present* 2023. doi:10.

21. Sparks, N. & Toumi, R. The Imperial College Storm Model (IRIS) Dataset. *Scientific data* **11,** 424 (2024).

22. Weiss, D. *et al.* Global maps of travel time to healthcare facilities. *Nature medicine* **26,** 1835–1838 (2020).

23. OpenStreetMap contributors. *Planet dump retrieved from https://planet.osm.org* `https://www.openstreetmap.org`. 2024.

24. Wang, X., Meng, X. & Long, Y. Projecting 1 km-grid population distributions from 2020 to 2100 globally under shared socioeconomic pathways. *Scientific Data* **9,** 563 (2022).

25. Thrasher, B. *et al.* NASA Global Daily Downscaled Projections, CMIP6. *Sci Data* **9,** 262. ISSN: 2052-4463 (Electronic) 2052-4463 (Linking) (2022).

26. . *Downscaling future and past climate data from GCMs* https://worldclim.org/data/downscaling.html. 2024.

27. Gething, P. W. *et al.* Modelling the global constraints of temperature on transmission of Plasmodium falciparum and P. vivax. *Parasit Vectors* **4,** 92. ISSN: 1756-3305 (Electronic) 1756-3305 (Linking) (2011).

28. Stopard, I. J., Churcher, T. S. & Lambert, B. Estimating the extrinsic incubation period of malaria using a mechanistic model of sporogony. *PLoS computational biology* **17,** e1008658 (2021).

29. Suh, E. *et al.* Estimating the effects of temperature on transmission of the human malaria parasite, Plasmodium falciparum. *Nature Communications* **15,** 3230 (2024).

30. Shapiro, L. L. M., Whitehead, S. A. & Thomas, M. B. Quantifying the effects of temperature on mosquito and parasite traits that determine the transmission potential of human malaria. *PLoS Biol* **15,** e2003489. ISSN: 1544-9173 (Print) 1544-9173 (2017).

31. Imbahale, S. S. *et al.* A longitudinal study on Anopheles mosquito larval abundance in western Kenya highlands. *Malaria Journal* **10,** 81 (2011).

32. Eckhoff, P. A. A malaria transmission-directed model of mosquito life cycle and ecology. *Malar J* **10,** 303. ISSN: 1475-2875 (Electronic) 1475-2875 (Linking) (2011).

33. McCann, R. S. *et al.* Aquatic habitats of the malaria vector *Anopheles funestus* in rural Malawi. *Malaria Journal* **19,** 1–12 (2020).

34. Tusting, L. S. *et al.* Housing Improvements and Malaria Risk in Sub-Saharan Africa: A Multi-Country Analysis of Survey Data. *PLoS Med* **14,** e1002234. ISSN: 1549-1676 (Electronic) 1549-1277 (Print) 1549-1277 (Linking) (2017).

35. Bhatt, S. *et al.* The effect of malaria control on Plasmodium falciparum in Africa between 2000 and 2015. *Nature* **526,** 207–211. ISSN: 1476-4687 (Electronic) 0028-0836 (Print) 0028-0836 (Linking) (2015).

36. World Health Organization. *World Malaria Report 2023* https://iris.who.int/handle/10665/374472 (World Health Organization, Geneva, Switzerland, 2023).

37. Sinka, M. E. *et al.* Modelling the relative abundance of the primary African vectors of malaria before and after the implementation of indoor, insecticide-based, vector control. *Malaria Journal* **15,** 142 (2016).

38. Tusting, L. S. *et al.* Mapping changes in housing in sub-Saharan Africa from 2000 to 2015. *Nature* **568,** 391–394. ISSN: 1476-4687 (Electronic) 0028-0836 (Print) 0028-0836 (Linking) (2019).

39. The DHS Program. *Demographic and Health Surveys (DHS)* various. https://www.dhsprogram.com.

40. Rahimi, A. & Recht, B. *Random Features for Large-Scale Kernel Machines* in *Advances in Neural Information Processing Systems (NIPS)* **20** (2007), 1177–1184. https://people.eecs.berkeley.edu/~brecht/papers/07.rah.rec.nips.pdf.

41. Smith, D. L., Guerra, C. A., Snow, R. W. & Hay, S. I. Standardizing estimates of the Plasmodium falciparum parasite rate. *Malaria Journal* **6,** 131 (2007).

42. Mappin, B. *et al.* Standardizing Plasmodium falciparum infection prevalence measured via microscopy versus rapid diagnostic test. *Malar J* **14,** 460. ISSN: 1475-2875 (Electronic) 1475-2875 (Linking) (2015).

43. Weiss, D. J. *et al.* Mapping the global prevalence, incidence, and mortality of *Plasmodium falciparum*, 200017: a spatial and temporal modelling study. *The Lancet* **394,** 322–331 (2019).

44. Bhatt, S. *et al.* Improved prediction accuracy for disease risk mapping using Gaussian process stacked generalization. *Journal of the Royal Society Interface* **14,** 20170520 (2017).

45. Simpson, D., Rue, H., Riebler, A., Martins, T. G. & Srbye, S. H. Penalising Model Component Complexity: A Principled, Practical Approach to Constructing Priors. *Statistical Science* **32,** 1–28 (2017).

46. Weiss, D. J. *et al.* Mapping the global prevalence, incidence, and mortality of *Plasmodium falciparum* and *Plasmodium vivax* malaria, 200022: a spatial and temporal modelling study. *The Lancet* **405,** 979–990 (2025).

47. Rue, H., Martino, S. & Chopin, N. Approximate Bayesian inference for latent Gaussian models by using integrated nested Laplace approximations. *Journal of the Royal Statistical Society: Series B (Statistical Methodology)* **71,** 319–392 (2009).

48. Lindgren, F., Rue, H. & Lindstrm, J. An explicit link between Gaussian fields and Gaussian Markov random fields: the stochastic partial differential equation approach. *Journal of the Royal Statistical Society: Series B (Statistical Methodology)* **73,** 423–498 (2011).

49. Gneiting, T. & Raftery, A. E. Strictly Proper Scoring Rules, Prediction, and Estimation. *Journal of the American Statistical Association* **102,** 359–378 (2007).

50. Masson-Delmotte, V. *et al.* Ipcc, 2021: Summary for policymakers. in: Climate change 2021: The physical science basis. contribution of working group i to the sixth assessment report of the intergovernmental panel on climate change (2021).

51. Trisos, C. *et al.* Africa. In: Climate Change 2022: Impacts, Adaptation and Vulnerability. Contribution of Working Group II to the Sixth Assessment Report of the Intergovernmental Panel on Climate Change (2022).

52. Cameron, E. *et al.* Defining the relationship between infection prevalence and clinical incidence of Plasmodium falciparum malaria. *Nat Commun* **6,** 8170. ISSN: 2041-1723 (Electronic) 2041-1723 (Linking) (2015).

53. R Core Team. *R: A Language and Environment for Statistical Computing* R version 4.2.1. R Foundation for Statistical Computing (Vienna, Austria, 2022). `https://www.R-project.org/`.

54. Golding, N. *et al. greta: Simple and Scalable Statistical Modeling in R* R package version 0.4.3.9 (2022). `https://greta-stats.org/`.

55. Wood, S. N. *mgcv: Mixed GAM Computation Vehicle with Automatic Smoothness Estimation* R package version 1.8-40 (2022). `https://CRAN.R-project.org/package=mgcv`.

56. Ridgeway, G. *et al. gbm: Generalized Boosted Regression Models* R package version 2.1.8 (2022). `https://CRAN.R-project.org/package=gbm`.

57. Rue, H. *et al. R-INLA: Bayesian Analysis of Latent Gaussian Models using Integrated Nested Laplace Approximations* R package version 22.12.16 (2022). `https://www.r-inla.org/`.

58. Developers, P. *paws: Amazon Web Services ('AWS') SDK for R* R package version 0.7.0 (2022). `https://CRAN.R-project.org/package=paws`.

59. Wickham, H. *et al. tidyverse: Easily Install and Load the 'Tidyverse'* R package version 2.0.0 (2022). `https://CRAN.R-project.org/package=tidyverse`.

60. Wickham, H. *et al. ggplot2: Create Elegant Data Visualisations Using the Grammar of Graphics* R package version 3.5.1 (2022). `https://CRAN.R-project.org/package=ggplot2`.

61. Hijmans, R. J. *terra: Spatial Data Analysis* R package version 1.7-83 (2022). `https://CRAN.R-project.org/package=terra`.

62. Pebesma, E. *sf: Simple Features for R* R package version 1.0-18 (2022). `https://CRAN.R-project.org/package=sf`.

63. Hernangmez, D. *tidyterra: 'tidyverse' Methods and 'ggplot2' Helpers for 'terra' Objects* R package version 0.6.1 (2022). `https://CRAN.R-project.org/package=tidyterra`.

64. Kassambara, A. *ggpubr: 'ggplot2' Based Publication Ready Plots* R package version 0.6.0 (2022). `https://CRAN.R-project.org/package=ggpubr`.

65. Wilke, C. O. *ggtext: Improved Text Rendering Support for 'ggplot2'* R package version 0.1.2 (2022). `https://CRAN.R-project.org/package=ggtext`.

66. Wilke, C. O. *ggridges: Ridgeline Plots in 'ggplot2'* R package version 0.5.6.9000 (2022). `https://CRAN.R-project.org/package=ggridges`.

67. Berger, F. *khroma: Colour Schemes for Scientific Data Visualization* R package version 1.7.0 (2022). `https://CRAN.R-project.org/package=khroma`.

68. Pedersen, T. L. & Crameri, F. *scico: Colour Palettes Based on the Scientific Colour-Maps* R package version 1.3.0 (2022). `https://CRAN.R-project.org/package=scico`.

69. Salmon, M. *NatParksPalettes: Color Palettes Inspired by National Parks* R package version 0.1.0 (2022). `https://CRAN.R-project.org/package=NatParksPalettes`.

70. Garnier, S. *viridis: Colorblind-Friendly Color Maps for R* R package version 0.6.2 (2022). `https://CRAN.R-project.org/package=viridis`.

71. Stopard, I. J., Churcher, T. S. & Lambert, B. Estimating the extrinsic incubation period of malaria using a mechanistic model of sporogony. *PLoS Comput Biol* **17,** e1008658. ISSN: 1553-7358 (Electronic) 1553-734X (Print) 1553-734X (Linking) (2021).

72. Tusting, L. S. *et al.* Mapping changes in housing in sub-Saharan Africa from 2000 to 2015. *Nature* **568,** 391–394. ISSN: 1476-4687 (Electronic) 0028-0836 (Print) 0028-0836 (Linking) (2019).